Contrib Mineral Petrol (2001) 142: 261–283
DOI 10.1007/s004100100293

James F. Luhr

Glass inclusions and melt volatile contents at Parícutin Volcano, Mexico

Received: 28 December 2000 / Accepted: 11 June 2001 / Published online: 17 August 2001

Abstract Olivine-hosted glass inclusions were investigated from tephra samples erupted at Parícutin volcano on four different dates: May 26 and August 1, 1943; January 23, 1945; and March 31, 1948. These dates span the first two thirds of the 9 year eruption, during which time the tephra/lava mass-eruption rate fell dramatically. They also span the strong whole-rock compositional shift of 1947, attributed to the increased importance of crustal contamination. Nine of the 26 analyzed glass inclusions have lower SiO_2 contents than any previously analyzed Parícutin lava sample, ranging to below 53 wt%. These silica-poor glasses are found in olivines erupted in 1943 and 1945, and provide evidence for melts that are parental to the main Parícutin lava suite. Total water contents in the glass inclusions measured by Fourier transform infrared (FTIR) spectroscopy vary considerably in all individual samples, with a total range of 1.8–4.0 wt%. Total water contents are not correlated with SiO_2 of the glass, Mg# of the adjacent host olivine, or eruption date. Only two glass inclusions have carbonate contents (248 and 296 ppm CO_2) above the FTIR detection limit of ~50 ppm CO_2; importantly, these inclusions also have the highest total water contents and among the highest SO_3^t values. These two inclusions were trapped at minimum depths of 9.0–9.6 km beneath the volcano. Thus, early degassing likely stripped most carbon from Parícutin melts at mid-crustal levels. Other glass inclusions yield minimum entrapment depths of 1.3–5.1 km based on water solubility limits. Total sulfur (0.30 to 0.01 wt% SO_3) declines as SiO_2 contents increase from 52.7 to 60.5 wt%. This trend and the wide range of glass inclusion total water contents are interpreted to reflect degassing accompanied by fractional crystallization and assimilation at upper crustal levels.

J.F. Luhr
Department of Mineral Sciences, NHB-119,
Smithsonian Institution, Washington, D.C. 20560, USA
E-mail: luhr@volcano.si.edu
Tel.: +1-202-3574809
Fax: +1-202-3572476

Editorial responsibility: T.L. Grove

Introduction

The eruption of Parícutin volcano in the west-central part of the Mexican Volcanic Belt (Fig. 1) was an important event for both volcanology and igneous petrology. From its birth in a Mexican cornfield on February 20, 1943, until its death on February 25, 1952, the complex evolution of the cinder cone and its associated lava field were documented in unprecedented detail (Kennedy 1946; Krauskopf and Williams 1946; Segerstrom and Gutiérrez 1947; Wilcox 1947a, 1947b, 1948a, 1948b; Wilcox and Gutiérrez 1948; Wilcox and Shoup-Oropeza 1948; Fries and Gutiérrez 1950a, 1950b, 1951a, 1951b, 1952a, 1952b, 1954; Foshag and González-Reyna 1956; summaries in Luhr and Simkin 1993). Pyroclastic activity was especially vigorous during the early years of the eruption, when the total eruptive rate was highest (Fig. 2). Significant ashfalls were recorded in Mexico City, 320 km to the east, only during March–July, 1943. Fries (1953) analyzed the masses of pyroclastic material and lava through the course of the eruption and concluded that the total mass-eruption rate fell dramatically during the early years. The tephra mass-eruption rate was ~5 times the lava rate for 1943, by 1947 the two were about equal, and thereafter the lava mass-eruption rate was 4–5 times that for tephra (Fig. 3).

Petrological studies by Wilcox (1954) demonstrated that the lavas of Parícutin evolved over time from early basaltic andesites with 55 wt% SiO_2 and phenocrysts (>0.3 mm) of olivine and rarer plagioclase, toward late-stage andesites with 60 wt% SiO_2 and phenocrysts of orthopyroxene. In 1947, about halfway through the eruption, when the mass-eruption rates of tephra and lava were about equal, the rate of compositional change was particularly rapid. Wilcox used graphical–chemical techniques to demonstrate that fractional crystallization

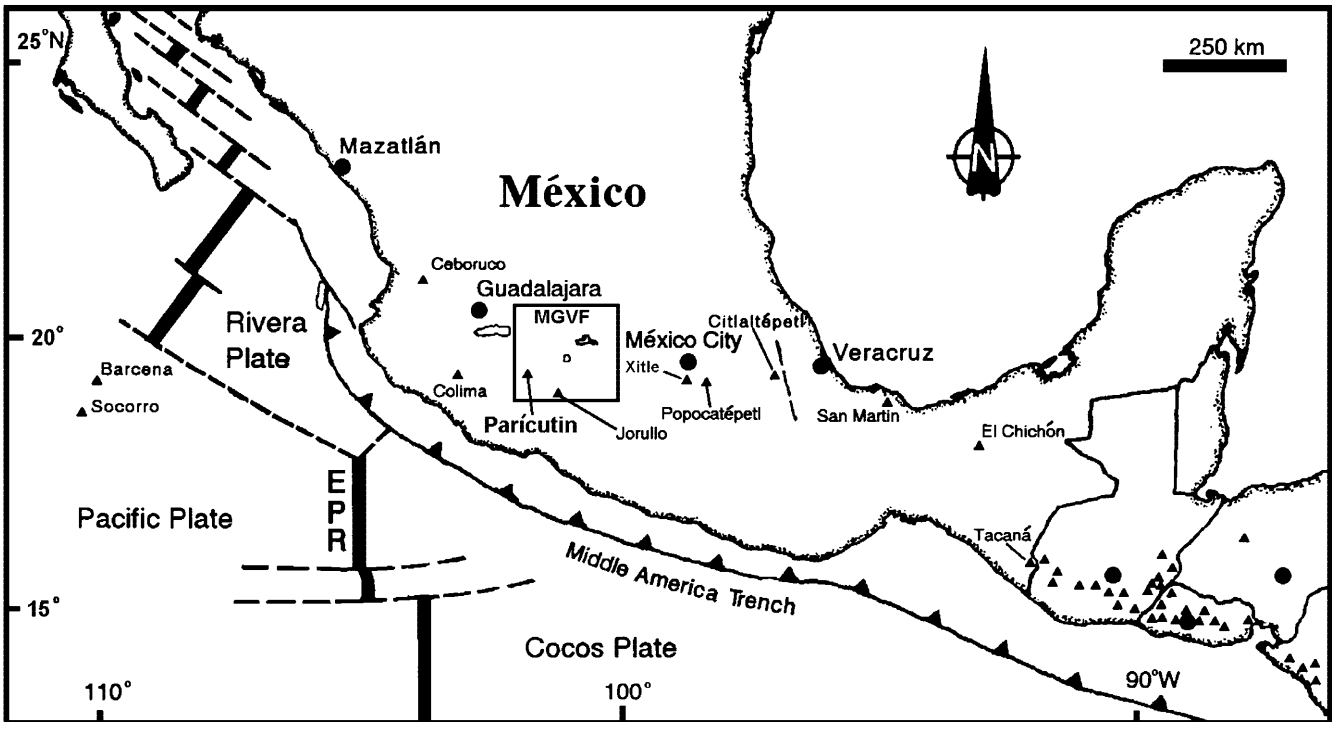

Fig. 1 Location map for Parícutin volcano, showing the E–W-trending Mexican Volcanic Belt, the northwestern end of the Central American Volcanic Belt, and principal plate-tectonic elements of the adjacent Pacific Ocean basin. *Dots* are major cities, with those in Mexico labeled. *Triangles* are volcanoes that have been active in the last 10,000 years, with those in Mexico labeled. *Large rectangle* marks the Michoacán–Guanajuato Volcanic Field (*MGVF*), in which Parícutin volcano is located. Offshore the Rivera, Pacific, and Cocos plates are indicated. The *thick dark lines* show the segmented East Pacific Rise (*EPR*) oceanic spreading ridges

alone was incapable of explaining these changes, but that when combined with assimilation of basement granitic rocks, satisfactory fits of the major element data could be obtained. This pioneering study presaged later computer-based assimilation–fractional crystallization models (DePaolo 1981). Subsequent analyses of trace elements and Sr and O isotopic ratios in many of the same lava specimens (McBirney et al. 1987) strongly supported the interpretations of Wilcox (1954), and have strengthened Parícutin's status as a classic example of assimilation–fractional crystallization in a subduction-related, calc-alkaline suite.

This study presents compositional data for glass inclusions trapped in olivine phenocrysts from Parícutin tephra erupted at four successive times: May, 1943; August, 1943; January, 1945; and March 1948 (Fig. 3). Abundances of major elements and volatile components in the glass inclusions were determined by electron microprobe and Fourier transform infrared (FTIR) spectroscopy. Electron microprobe data are also presented for host olivines and matrix glasses of the scoriae. These data are used to assess changes in the glass and olivine compositions over time, particularly with regard to the evidence for enhanced assimilation in magmas erupted during and after 1947, and possible controls on eruptive style dictated by changes in melt volatile content.

Samples investigated, textures, and techniques

Selection criteria

The U.S. National Rock and Ore Collection at the Smithsonian contains the world's best assembly of material from the Parícutin eruption, including all of the lavas studied by Wilcox (1954), as well as extensive lava and tephra samples collected by William Foshag Jr. and other geologists. Foshag was a curator at the Smithsonian from 1929 until his death in 1956. He and colleague Jenaro González-Reyna from the Mexican National University wrote the classic account of Parícutin's birth and the eruption's early years (Foshag and González-Reyna 1956). Among the Smithsonian's extensive holdings for Parícutin, however, few samples are suitable for studies aimed at analysis of water, hydroxyl, and carbon species in quenched glass inclusions. Four criteria were considered essential for consideration of a sample in this study:

1. The sample consists of vesicular scoria or ash, less than 3 cm in diameter, to assure rapid quenching in the atmosphere and minimal post-eruptive crystallization of the trapped melt either to the host crystal wall or to daughter crystals. Slowly cooled lava samples, which dominate the Smithsonian's Parícutin collections, and were the entire focus of the studies by Wilcox (1954) and McBirney et al. (1987), are inappropriate to glass inclusion studies, unless rehomogenized at high temperature in the laboratory.

Fig. 2 "Heavy cineritic activity" at Parícutin Volcano on May 24, 1943, two days before eruption of the earliest scoria sample included in this study (108135). Photo by William Foshag taken from Cerro de Jarátiro, 1 km north of the new volcano

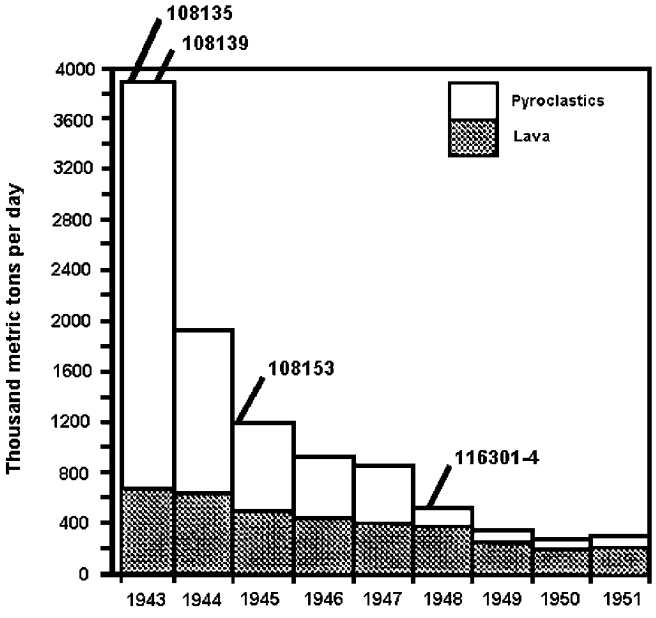

Fig. 3 Average daily weights of pyroclastic material and lava erupted at Parícutin, by years, 1943–1951, with data taken from Fries (1953). The tephra mass-eruption rate fell dramatically during the course of the eruption, whereas the lava mass-eruption rate declined very slowly. *Thick leader lines* to sample numbers indicate the times of eruption for the four tephra samples investigated in this study

2. The eruption date is known with confidence. Thus, the tephra were either collected as they fell, or were collected in rain gauges or on other human-made surfaces.
3. Sufficient material existed to allow 20–30 g to be destructively processed to extract olivine phenocrysts.
4. This study was restricted to olivine-hosted glass inclusions. Orthopyroxene largely replaced olivine as the stable mafic phenocryst in 1947, although minor olivine continued to be present until the end of the eruption in 1952. The strong cleavage in orthopyroxene led to repeated failures in attempts to prepare orthopyroxene-hosted glass inclusions, and caused grave doubts about the ability of orthopyroxene to preserve volatile-rich glass inclusions.

Only four samples (given by U.S. National Museum numbers) passed all four of these criteria:

- 108135: vesicular scoriae up to 2.5 cm in size erupted on May 26, 1943. Collected by William Foshag, Jr. at the foot of the lava flow on the northeast side of the Parícutin lava field.
- 108139: strongly vesicular scoriae up to 2 cm in size erupted on August 1, 1943. Collected by William Foshag, Jr.
- 108153: vesicular scoriae up to 2.5 cm in size erupted on January 23, 1945. Collected by William Foshag, Jr.
- 116301-4: bulk sample of ~1-mm-thick ash layer erupted on March 31, 1948. It was collected at the Jarátiro triangulation station, 2 km north of Parícutin volcano, by Ray Wilcox. The largest fragments of vesicular scoriae are ~3 mm in size.

The first three samples were erupted prior to the dramatic shift in lava compositions in 1947. Ash sample 116301-4 erupted in March 1948 in the midst of those assimilation-related compositional changes.

Textures and modes

Modes of the four studied samples were determined by conventional point counting (Table 1). Olivine phenocrysts (> 0.3 mm) are present in all four samples at 4.0 to 0.2 vol%, declining crudely with time. Olivine phenocrysts reach maximum sizes of 0.6 mm (samples 108139 and 116301-4) to 1.2 mm (samples 108135 and 108153). They contain abundant cubes of brown Cr-rich spinel, 5–20 μm across, which are either isolated, in clusters, or in chains. Similar inclusion textures and compositions for spinels in Parícutin lava samples were discussed in detail by Bannister et al. (1998), who also presented the first electron microprobe analyses of spinel, olivine, and orthopyroxene in Parícutin lavas. Many olivine crystals in both lavas and scoriae of Parícutin show skeletal morphologies, which are intimately related to the trap-

Table 1 Modes of Parícutin scoria and ash samples

USNM no.	108135	108139	108153	116301-4
Point counting (vol%)[a]				
Oliv ph	4.0	1.6	2.2	0.2
Oliv mp	1.8	3.5	2.7	0.8
Plag mp	8.5	14.6	9.7	8.7
Opx mp	0.0	0.0	0.0	2.8
Matrix	85.7	80.3	85.4	87.5
Least-squares models (wt%)[b]				
Oliv	9.6	7.5	8.9	6.0
Plag	32.6	27.0	29.9	30.7
Opx	0.0	0.0	0.0	2.2
Glass	57.8	65.5	61.2	61.1
Σr^2	0.49	0.41	0.39	0.53
Least-squares models (vol%)[b]				
Oliv	7.6	5.9	7.0	4.6
Plag	32.7	26.7	29.7	29.7
Opx	0.0	0.0	0.0	1.7
Glass	59.7	67.4	63.3	64.0

[a] *Point counting*: more than 500 points counted in combined reflected and cross-polarized transmitted light on a single polished thin section for each sample. Mineral abbreviations: *Oliv* olivine, *Plag* plagioclase, *Opx* orthopyroxene. Textural abbreviations: *ph* phenocryst (>0.3 mm); *mp* microphenocryst (>0.03 mm, <0.3 mm); Matrix (<0.03 mm: after Wilcox 1954)

[b] *Least-squares models*: calculated using matrix glass compositions (Table 5) and compositions of microphenocrystic olivine, plagioclase, and orthopyroxene. Relatively high values for the sum of residuals squared (Σr^2) reflect poor fits for Na_2O, which the models predict to be higher than measured in the matrix glasses. Wt% modes were converted to vol% modes assuming densities of 3,400 g/l for olivine and orthopyroxene, 2,700 g/l for plagioclase, and 2,530–2,620 g/l for glasses, which were calculated individually as discussed in the text, assuming they are anhydrous

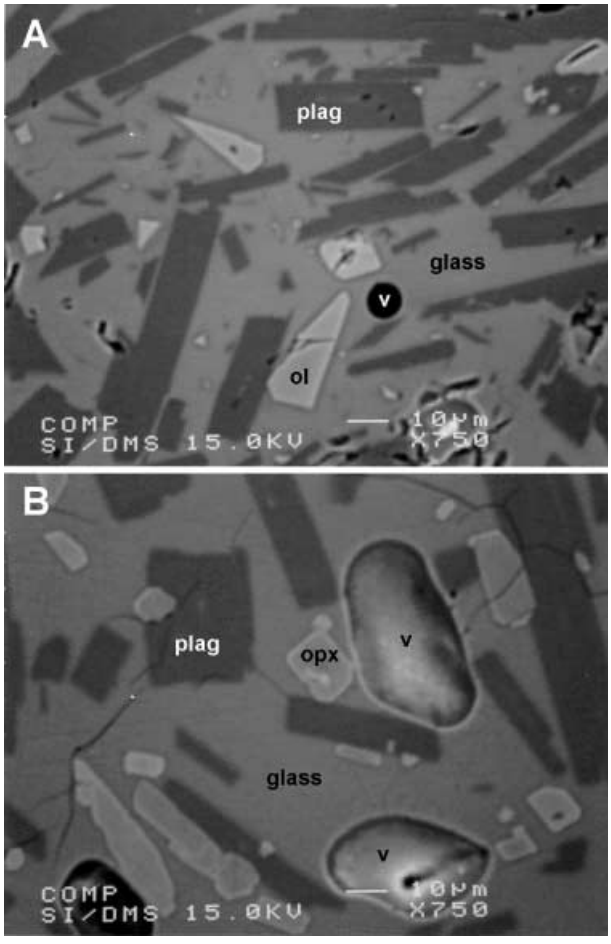

Fig. 4 Backscattered electron images of representative matrix areas in two Parícutin scoriae: **a** 108135, erupted in May 1943, shows microphenocrysts and microlites of plagioclase (*plag*) and olivine (*ol*) surrounded by glass with a vesicle (*v*); **b** 116301-4, erupted in March 1948, shows microphenocrysts and microlites of plagioclase (*plag*) and orthopyroxene (*opx*) surrounded by glass with vesicles (*v*). Scale is shown by 10 μm bar

ping of some types of glass inclusions. Because many of these inclusions remained connected to the matrix melt throughout crystal growth, and undoubtedly degassed during ascent and eruption, they were not analyzed in this study, which focused on pre-eruptive volatile contents.

The olivine phenocrysts are surrounded by a matrix consisting of glass studded with microphenocrysts (>0.03 mm, <0.3 mm) and microlites (<0.03 mm) of plagioclase and olivine, except in the last-erupted sample (116301-4) where orthopyroxene is present as microphenocrysts and microlites instead of olivine. Representative matrix textures of samples 108135 and 116301-4 are shown in Fig. 4a and b, respectively. Plagioclase laths are mostly less than 150×20 μm in size, but rarely reach lengths of 500 μm. Most olivine and orthopyroxene crystals in the matrix have long dimensions of 10–30 μm. Bannister et al. (1998) concluded that titanomagnetite found in the matrix of Parícutin lavas crystallized after extrusion. The lack of titanomagnetite in the quickly quenched scoriae of this study supports that interpretation.

Modes were also calculated for the four scoria/ash samples using least-squares techniques to fit the bulk major element compositions to those of the matrix glass and microphenocrystic olivine, plagioclase, and orthopyroxene. The least-squares models were calculated in wt%, and then converted to vol% (Table 1). The modes determined by point counting are very different from the calculated modes. In the former approach, glass plus all microlites (<0.03 mm) are counted as matrix, whereas all crystals of any size are counted in the least-squares models. The least-squares approach also has the limitation that a single representative composition must be used for each mineral, even when significant core–rim compositional zoning is present.

The textures and mineral assemblages described here differ somewhat from those discussed by Wilcox (1954) and Bannister et al. (1998), again owing primarily to differences in the nature of the samples studied: quickly quenched scoria/ash samples in this study versus more slowly quenched and degassed lavas. In lava samples erupted after 1944, olivine phenocrysts have reaction coronae of fine-grained orthopyroxene. These coronae must have formed after eruption as the mostly degassed lavas cooled relatively slowly at Earth's surface, because they are not evident in the quickly quenched

scoriae of this study, including sample 116301-4 erupted in 1948, which has orthopyroxene instead of olivine in the matrix. Similarly, Wilcox (1954) and Bannister et al. (1998) described and analyzed clinopyroxene and orthopyroxene microphenocrysts and microlites in many samples erupted during 1943–1948. In contrast, no clinopyroxene was encountered in this study, and the only orthopyroxene was found as microphenocrysts and microlites in sample 116301-4, erupted in 1948, where no microphenocrysts or microlites of olivine are present.

Descriptions of the analyzed glass inclusions are given in Table 2. The nature of the largest isolated glass inclusions in olivine changed during the course of the Parícutin eruption. In the earliest erupted samples, some olivine crystals contain two opposing, conical volumes of glass aligned along the olivine *a*-axis to form an hourglass configuration (Fig. 5). The largest individual glass cones, halves of an hourglass pair, have cone heights of 100–250 μm and basal diameters of 50–180 μm. This hourglass texture is quite distinct from the texture of the same name discussed by Anderson (1991) for rim-connected glass inclusions in quartz crystals from the Bishop Tuff. It should be noted, however, that use of the term ''hourglass'' has precedence at Parícutin, where these textures were described with the Spanish equivalent ''reloz de arena'' by Schmitter (1943) in the year of Parícutin's birth. As the Parícutin eruption evolved, these hourglass textures became less important and *a*-axis-parallel, long and narrow rod and prismatic shapes (Fig. 5) came to dominate among the largest glass inclusions. In most olivines from all stages of the eruption, smaller ellipsoidal to spherical glass inclusions are also present (Fig. 5).

For most of the glass inclusions listed in Table 2, the vapor bubble diameter is given along with an estimate of the vol% of the inclusion occupied by the vapor bubble. In most cases the spherical bubble volumes could be accurately estimated. The greater source of uncertainty for the bubble vol% is the volume of the glass inclusion itself, which can be complicated by irregular inclusion shapes and is probably only known to $\pm 20\%$. Typical glass inclusions contain a single bubble that represents 2–6 vol% of the inclusion. Two of the studied inclusions contain two bubbles each. In three inclusions the bubble volumes represent 8–14% of the inclusion. Two of the glass inclusions listed in Table 2 contain a few spinel crystals, similar to those within the host olivine; these glass compositions show no abnormalities with regard to Fe or Ti trends, and therefore the spinels were likely

Table 2 Descriptions of Parícutin glass inclusions analyzed by electron microprobe

Inclusion	Shape	Type	Size (μm)[a]	Vapor bubble diameter (μm)[b]	Vapor bubble (vol%)[b]	Crystals
108135-A	Cone	Hourglass	180, 80	28	3.1	None
108135-B	Cone	Hourglass	185, 100	33	4.0	None
108135-C	Pyramid	Flat hourglass	225, 110, 60	35	4.6	Spinel
108135-D	Cone	Hourglass	185, 60	27	5.8	None
108139-A	Ellipsoid	–	185, 165, 165	50, 24	2.3, 0.3	None
108139-E	Rectangular prism	*a*-axis	540, 35, 17	30	4.4	None
108139-G	Cone	Hourglass	135, 75	12	2.3	None
108139-J1	Rectangular prism	*a*-axis	220, 25, 25	22	5.2	None
108139-J2	Cone	Hourglass	115, 50	20	2.2	None
108153-A	Cone	Hourglass	200, 180	64	8.1	None
108153-C	Triangular prism	–	365, 70, 45	47	10.0	None
108153-D	Triangular prism	–	145, 120, 50	36	5.6	None
108153-F	Triangular prism	–	200, 135, 35	30	3.0	None
108153-H	Rod	*a*-axis	250, 32	?[c]	?	None
108153-I	Triangular prism	–	260, 134, 30	50, 26	12.5, 1.8	None
108153-J	Triangular prism	–	125, 65, 55	?	?	None
108153-Ka	Rod	*a*-axis	300, 38	?	?	None
108153-Kb	Irregular	–	300, 100, 30	?	?	None
108153-Kc	Irregular	–	150, 120, 20	?	?	Spinel
108153-La	Pyramid	–	76, 155, 150	30	2.4	None
108153-Lb	Irregular	–	100, 88, 67	?	?	None
116301-4b	Ellipsoid	–	160, 90, 45	30	2.9	None
116301-4D	Triangular prism	–	350, 57, 123	?	?	Minor devitrification
116301-4E	Rod	–	115, 35	22	5.1	None
116301-4F	Rectangular prism	Hourglass	80, 65, 20	18	2.9	None
116301-4H	Rod	–	175, 53	25	2.1	None

[a] *Size*: for cone shape x, y are cone height, basal diameter; for pyramid shape x, y, z are height, base1, base2; for ellipsoid shape x, y, z are the three principal diameters; for rectangular prism x, y, z are length, base1, base2; for triangular prism x, y, z are length, triangle base, triangle height; for rod shape x, y are length, basal diameter; and for irregular shape x, y, z reflect the three major dimensions

[b] *Vapor bubble diameter and vol%* : where two values are listed (x, y), two different bubbles are present and separate values are reported for each

[c] Interrogation marks (?) indicate inclusions for which bubble sizes were not measured

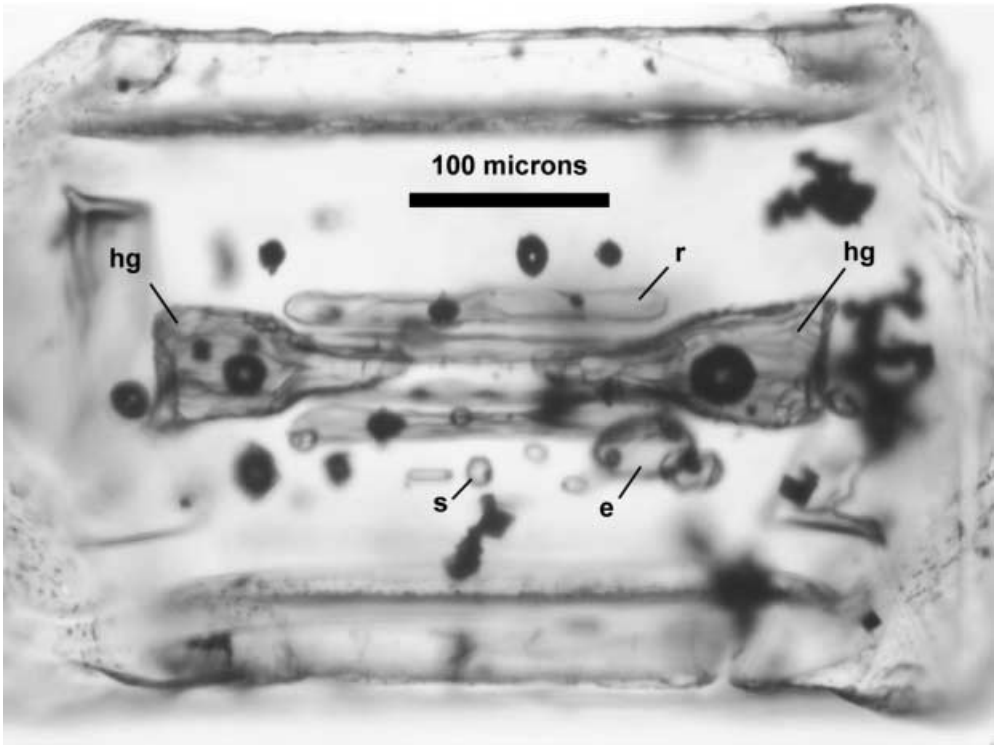

Fig. 5 An olivine crystal from sample 108135 shows examples of the different glass inclusion types present in Parícutin olivines: a pair of symmetrical pyramid-shaped glass inclusions form an hourglass (*hg*) structure that lies along the crystal's central *a*-axis; several rod-shaped glass inclusions (*r*) are also parallel to the *a*-axis; various small spherical (*s*) and ellipsoidal (*e*) glass inclusions are also present. All of the glass inclusions labeled contain a single vapor bubble. The crystal was photographed in plane light on a petrographic microscope while lying in immersion oil with refractive index of 1.67

trapped along with the glass rather than forming as post-entrapment precipitates. Another glass inclusion showed minor devitrification. All other glass inclusions were free of crystals.

Preparation of wafers for glass inclusion analysis

Approximately 30 g of each tephra sample (either small scoriae or fine–medium ash) were cleaned in distilled water, dried, and repeatedly crushed by hand in an agate mortar and pestle and passed through a 0.5 mm sieve to be caught in a 0.335 mm sieve. The 0.5–0.335 mm fraction was then washed in distilled water, dried, and olivine crystals were separated by sinking in saturated sodium polytungstate liquid ($\rho = 2.89$ g/cm^3). The separated olivine crystals were then leached in cold fluoboric acid (HBF_4) for 2 h, with several intermediate 5-min steps of ultrasonication. The purpose of this leaching was to remove exterior glass from the olivine crystals so that glass inclusions could be easily observed. Olivine crystals were then placed in a Petri dish in immersion oil with refractive index of 1.67, similar to the refractive index of olivine, and examined under a binocular microscope. In this immersion oil, the olivine grain boundaries are very faint and glass inclusions stand out dramatically for observation. The main criteria used for selection of glass inclusions for analysis were:

1. Size needed to be sufficient to allow preparation of a wafer with glass at least 40 μm thick and 25 μm across in the other two dimensions. The size criterion eliminated the great majority of glass inclusions, which are smaller than 25 μm.
2. Absence of cracks into the inclusion from the surrounding crystal was taken to indicate that the inclusion had not leaked prior to eruptive quenching.

Selected crystals were then digitally photographed in oil (Fig. 5), removed, and cleaned in acetone. Crystals were encased in thermoplastic on a glass slide heated on a hotplate, and then oriented under a binocular microscope. The upper end of the oriented crystal was then ground flat on an Ingram grinder, and the grinding was continued by hand on 600 μm grit paper until the desired level in the glass inclusion was nearly reached. The crystal was then removed from the thermoplastic, cleaned in acetone, and the flat surface was stuck to a piece of double-sided tape, surrounded by a mold, and encased in epoxy plus silicon carbide grit filler. Once set, the epoxy-grit puck with crystal was removed from the mold, ground slightly on the 600 μm grit paper until the desired final level was reached in the glass inclusion, and polished using 6 μm diamond paste and 0.3 μm diamond suspension. The polished glass inclusion was then digitally photographed, the puck was carbon-coated, and electron microprobe analyses were conducted on the glass inclusion and adjacent olivine, as described below. The reason for removing the oriented crystal from the thermoplastic mount and encasing it in the epoxy-grit puck, was to assure that the polished surface of the crystal and glass inclusion were exactly perpendicular to the electron microprobe beam, a condition that could not be reliably achieved in the thermoplastic mount.

Following electron microprobe analysis, the carbon coat was removed on the 0.3 μm lap, and the puck was sawn into a cube ~8 mm on a side. The polished surface

was attached to a glass slide with thermoplastic, and the back side of the cube was then ground down to nearly intersect the crystal using the Ingram grinder. Grinding was continued by hand on the 600 μm grit paper until the second side of the glass inclusion reached the desired level. The second side was then polished as described above. The mount was then soaked in acetone to remove the doubly polished wafer, which consisted of the crystal with inclusion and a surrounding square of epoxy plus silicon carbide grit.

Analytical methods

X-ray fluorescence spectrometry and inductively coupled plasma mass spectrometry

Bulk analyses were conducted for the four Parícutin tephra samples investigated in this study. About 30 g of each sample were cleaned in distilled water, dried, and powdered in an alumina shatterbox. These powders were analyzed by X-ray fluorescence (XRF) spectroscopy and inductively coupled plasma mass spectrometry (ICP-MS). The data are listed in Table 3.

Electron microprobe analysis

All electron microprobe analyses were conducted on the Smithsonian's JEOL-8900 instrument at 15 kV accelerating potential. Table 4 presents electron microprobe analyses for 26 different glass inclusions, representing 22 different olivine crystals. Table 5 lists average matrix

Table 3 Bulk analyses of Parícutin scoria and ash samples

USNM no.	108135	108139	108153	116301-4
Date erupted	May 26, 1943	August 1, 1943	January 23, 1945	March 31, 1948
Mass%	15	28	56	84
XRF (wt%)				
SiO_2	54.74	55.92	55.64	58.50
TiO_2	0.93	0.97	1.03	0.82
Al_2O_3	18.26	17.86	17.47	17.45
Fe_2O_3	2.37	2.12	2.03	2.18
FeO	5.00	5.07	5.25	4.23
MnO	0.12	0.12	0.13	0.11
MgO	5.75	5.36	5.66	4.41
CaO	7.44	7.01	6.94	6.43
Na_2O	4.27	4.36	4.33	4.30
K_2O	0.87	1.22	1.33	1.48
P_2O_5	0.29	0.33	0.36	0.30
LOI	–0.24	–0.24	–0.09	0.01
Total	99.80	100.11	100.07	100.21
XRF ppm				
V	135	131	134	110
Cr	163	153	177	102
Co	29	27	29	24
Ni	109	88	117	76
Cu	41	37	36	29
Zn	90	84	88	103
Rb	10	17	19	23
Sr	603	589	583	550
Y	16	18	20	18
Zr	187	222	268	245
Nb	10	9	13	12
Ba	276	351	381	449
ICP-MS (ppm)				
Sc	20.2	20.1	20.1	16.8
Rb	9.0	15.6	17.0	21.0
Sr	599	613	592	536
Y	17.50	19.87	21.64	18.40
Zr	98	133	155	144
Nb	4.74	8.23	10.04	7.14
Cs	0.31	0.46	0.43	0.57
Ba	290	365	396	469
La	11.86	16.26	19.02	18.00
Ce	24.33	32.46	37.46	35.22
Pr	3.14	4.02	4.60	4.30
Nd	14.17	17.73	19.63	18.23
Sm	3.60	4.20	4.67	4.25
Eu	1.19	1.37	1.49	1.30
Gd	3.45	3.99	4.32	3.85
Tb	0.55	0.63	0.68	0.61
Dy	3.29	3.75	4.07	3.54
Ho	0.66	0.74	0.82	0.70
Er	1.75	1.98	2.14	1.88
Tm	0.26	0.28	0.30	0.27
Yb	1.60	1.78	1.93	1.62
Lu	0.24	0.28	0.30	0.26
Hf	2.68	3.39	3.95	3.73
Ta	0.30	0.53	0.67	0.48
Pb	4.60	5.92	6.45	8.83
Th	0.89	1.51	1.78	1.76
U	0.31	0.49	0.53	0.51

XRF analyses were performed on the Smithsonian's Philips PW 1480 spectrometer. Major elements were determined on glass disks prepared from 9:1 mixtures of Li-tetraborate and rock powder that had been heated and oxidized during loss on ignition (LOI) determination. Precisions (1σ) were estimated by repeated analysis of one sample and correspond to the following values: SiO_2 = 0.26 wt%, TiO_2 = 0.02%, Al_2O_3 = 0.09%, $Fe_2O_3^{Total}$ = 0.22%, MnO = 0.01%, MgO = 0.08%, CaO = 0.02%, Na_2O = 0.06%, K_2O = 0.04%, and P_2O_5 = 0.01%. FeO was determined by K-dichromate titration following a modified version of the method of Peck (1964). Fe_2O_3 was then calculated from the XRF value for total iron. LOI values are loss on ignition measurements at 1,000 °C for 1 h on powders dried for several hours at 110 °C. These LOI values have not been corrected for oxygen uptake upon conversion of FeO to Fe_2O_3 in the furnace. Trace element analyses by XRF were determined at the Smithsonian on pressed disks made from mixtures of 1.6 g rock powder and 0.4 g cellulose, with a boric acid backing. Estimated 1σ precisions based on 59 analyses of BHVO-1 correspond to the following percentages of the amounts present: V (1), Cr (1), Co (1), Ni (1), Cu (2), Zn (2), Rb (10), Sr (1), Y (2), Zr (2), Nb (12), Ba (5). Trace element analyses by ICP-MS (inductively coupled plasma mass spectroscopy) were performed at Washington State University. Estimated 1σ precisions based on 50 analyses of sample BCR-P, or in the cases of Sr and Sc on 62 analyses of sample TED, correspond to the following percentages of the amounts present: Sc (3.5%), Rb (1.4), Sr (1.6), Y (0.8), Nb (2.2), Cs (3.1), Ba (1.9), La (1.9), Ce (1.2), Pr (1.0), Nd (1.8), Sm (2.1), Eu (1.9), Gd (1.1), Tb (1.1), Dy (1.3), Ho (1.5), Er (1.4), Tm (1.2), Yb (0.9), Lu (1.9), Hf (1.5), Ta (2.7), Pb (3.2), Th (9.5), U (9.3)

Table 4 Electron microprobe analyses of Parícutin glass inclusions

Sample	108135-A	108135-B	108135-C	108135-D	108139-A	108139-E	108139-G
No. spots	2	4	3	2	5	1	3
(wt%)							
SiO_2	50.72	51.68	51.46	51.12	52.45	50.27	50.81
TiO_2	0.96	0.94	0.86	1.00	0.98	1.03	0.91
Al_2O_3	16.95	17.49	17.78	18.22	16.61	18.81	16.25
FeO^t	7.20	7.42	7.58	7.93	7.01	7.38	6.79
MnO	0.12	0.13	0.15	0.16	0.13	0.20	0.13
MgO	4.35	5.47	4.61	4.58	5.10	3.87	4.88
CaO	7.26	7.34	7.74	7.78	6.78	7.65	6.55
Na_2O	3.61	3.57	3.66	3.88	3.65	4.06	3.54
K_2O	0.82	0.77	0.74	0.82	1.09	1.19	1.09
P_2O_5	0.25	0.23	0.27	0.27	0.26	0.32	0.26
Cl	0.10	0.10	0.10	0.10	0.09	0.11	0.09
SO_3^t	0.27	0.28	0.26	0.25	0.22	0.20	0.22
Total	92.61	95.45	95.21	96.13	94.37	95.09	91.52
(1σ)							
SiO_2	0.04	0.37	0.17	0.32	0.33	–	0.15
TiO_2	0.06	0.05	0.01	0.03	0.04	–	0.06
Al_2O_3	0.02	0.24	0.07	0.09	0.18	–	0.13
FeO^t	0.08	0.15	0.09	0.10	0.23	–	0.13
MnO	0.05	0.02	0.04	0.00	0.03	–	0.04
MgO	0.14	0.09	0.29	0.02	0.09	–	0.03
CaO	0.06	0.10	0.12	0.11	0.06	–	0.05
Na_2O	0.07	0.06	0.09	0.08	0.05	–	0.01
K_2O	0.08	0.02	0.04	0.02	0.05	–	0.03
P_2O_5	0.01	0.01	0.02	0.01	0.02	–	0.02
Cl	0.00	0.00	0.01	0.01	0.01	–	0.01
SO_3^t	0.00	0.00	0.00	0.01	0.00	–	0.00
CIPW norm (wt%)							
q	2.88	1.75	1.77	0.00	3.29	0.00	3.09
hy	18.35	21.67	19.29	17.83	19.97	9.01	19.98
ol	0.00	0.00	0.00	1.04	0.00	5.86	0.00
S-K_α peak position							
$\%S^{+6}$	69	46	65	87	105	35	58
1σ	14	8	17	11	20	17	22
Olivine-corrected glass analysis							
Wt% olivine	3	0	2	3	0	2	0
SiO_2	54.32	54.14	53.75	52.76	55.58	52.61	55.51
TiO_2	1.00	0.99	0.89	1.01	1.04	1.06	1.00
Al_2O_3	17.76	18.33	18.30	18.39	17.60	19.38	17.76
FeO^t	7.99	7.78	8.10	8.46	7.43	7.93	7.41
MnO	0.13	0.14	0.16	0.17	0.14	0.21	0.14
MgO	5.90	5.73	5.64	5.97	5.41	4.85	5.33
CaO	7.60	7.69	7.97	7.86	7.18	7.89	7.16
Na_2O	3.78	3.74	3.76	3.92	3.86	4.19	3.87
K_2O	0.86	0.81	0.76	0.83	1.15	1.23	1.19
P_2O_5	0.26	0.24	0.28	0.28	0.28	0.33	0.29
Cl	0.10	0.10	0.10	0.10	0.10	0.11	0.10
SO_3^t	0.29	0.30	0.27	0.25	0.23	0.20	0.24
Total	99.99	100.00	99.99	99.99	100.00	99.99	100.00

Sample	108139-J1	108139-J2	108153-A	108153-C	108153-D	108153-F	108153-H
No. spots	1	2	4	3	3	2	3
(wt%)							
SiO_2	52.39	52.11	52.48	53.61	53.02	53.20	59.33
TiO_2	0.93	1.04	0.98	0.97	1.13	1.04	1.62
Al_2O_3	17.44	18.02	16.45	17.10	19.09	16.94	14.83
FeO^t	7.28	7.43	6.64	7.63	7.20	6.81	7.04
MnO	0.15	0.14	0.13	0.12	0.12	0.12	0.13
MgO	5.07	4.50	4.95	5.25	3.99	5.10	3.25
CaO	6.84	6.63	6.90	6.76	7.68	6.96	5.77

Table 4 (Contd.)

Sample	108139-J1	108139-J2	108153-A	108153-C	108153-D	108153-F	108153-H
No. spots	1	2	4	3	3	2	3
Na_2O	3.75	3.84	3.41	3.62	4.44	3.75	4.24
K_2O	1.13	1.33	1.06	1.21	1.38	1.20	2.01
P_2O_5	0.29	0.29	0.40	0.31	0.32	0.32	0.44
Cl	0.09	0.09	0.09	0.08	0.10	0.08	0.08
SO_3^t	0.22	0.22	0.25	0.20	0.20	0.21	0.01
Total	95.59	95.63	93.74	96.85	98.66	95.73	98.73

Sample	108135-A	108135-B	108135-C	108135-D	108139-A	108139-E	108139-G
No. spots	2	4	3	2	5	1	3
(wt%)							
(1σ)							
SiO_2	–	0.30	0.53	0.32	0.20	0.07	0.20
TiO_2	–	0.00	0.05	0.04	0.03	0.02	0.05
Al_2O_3	–	0.19	0.18	0.24	0.06	0.09	0.12
FeO^t	–	0.15	0.21	0.34	0.09	0.01	0.20
MnO	–	0.00	0.02	0.02	0.02	0.03	0.03
MgO	–	0.05	0.15	0.15	0.04	0.03	0.06
CaO	–	0.15	0.04	0.05	0.14	0.06	0.12
Na_2O	–	0.02	0.09	0.23	0.05	0.04	0.03
K_2O	–	0.02	0.05	0.01	0.01	0.07	0.03
P_2O_5	–	0.00	0.07	0.01	0.03	0.01	0.02
Cl	–	0.00	0.00	0.01	0.01	0.00	0.00
SO_3^t	–	0.01	0.01	0.01	0.00	0.01	0.01
CIPW norm (wt%)							
q	1.79	1.15	5.29	3.25	0.00	3.01	9.83
hy	20.76	19.92	19.52	21.31	8.48	19.05	11.52
ol	0.00	0.00	0.00	0.00	5.11	0.00	0.00
S-K_α peak position							
$\%S^{+6}$	42	61	57	53	10	50	No peak
1σ	11	16	26	4	9	17	–
Olivine-corrected glass analysis							
Wt% olivine	0	1	0	0	2	0	4
SiO_2	54.81	54.33	55.98	55.35	53.46	55.57	59.25
TiO_2	0.98	1.08	1.05	1.00	1.12	1.09	1.57
Al_2O_3	18.24	18.65	17.55	17.65	18.96	17.70	14.42
FeO^t	7.62	7.85	7.08	7.87	7.47	7.11	7.49
MnO	0.16	0.14	0.14	0.12	0.12	0.12	0.13
MgO	5.30	5.10	5.28	5.42	4.84	5.33	4.92
CaO	7.16	6.86	7.36	6.98	7.63	7.27	5.61
Na_2O	3.92	3.97	3.64	3.74	4.41	3.92	4.12
K_2O	1.18	1.38	1.14	1.25	1.37	1.25	1.95
P_2O_5	0.30	0.30	0.42	0.32	0.31	0.33	0.42
Cl	0.10	0.09	0.09	0.08	0.10	0.09	0.07
SO_3^t	0.23	0.23	0.27	0.21	0.20	0.22	0.01
Total	100.00	100.00	100.00	100.00	99.99	100.00	99.99

Sample	108153-I	108153-J	108153-Ka	108153-Kb	108153-Kc	108153-La	108153-Lb
No. spots	3	3	2	2	1	3	3
(wt%)							
SiO_2	53.17	60.10	55.14	56.91	59.08	53.36	52.76
TiO_2	1.21	1.79	1.14	1.35	1.64	1.06	1.06
Al_2O_3	19.32	14.87	18.12	16.67	15.40	17.08	17.07
FeO^t	6.92	6.59	7.46	7.55	6.80	7.57	7.94
MnO	0.12	0.11	0.16	0.12	0.13	0.11	0.14
MgO	3.85	3.22	4.00	3.75	3.27	4.84	5.02
CaO	7.84	5.39	7.26	6.52	5.57	6.95	7.14
Na_2O	4.61	4.13	4.39	4.56	4.44	3.98	3.80
K_2O	1.35	1.84	1.62	1.71	1.82	1.26	1.13
P_2O_5	0.33	0.53	0.32	0.35	0.46	0.30	0.32
P_2O_5	0.33	0.53	0.32	0.35	0.46	0.30	0.32
Cl	0.09	0.10	0.11	0.10	0.10	0.09	0.09
SO_3^t	0.18	0.07	0.15	0.07	0.03	0.16	0.21
Total	98.99	98.74	99.87	99.67	98.73	96.77	96.67

Table 4 (Contd.)

Sample	108153-I	108153-J	108153-Ka	108153-Kb	108153-Kc	108153-La	108153-Lb
No. spots	3	3	2	2	1	3	3
1σ							
SiO_2	0.21	0.21	0.23	0.96	–	0.37	0.11
TiO_2	0.09	0.11	0.07	0.03	–	0.05	0.08
Al_2O_3	0.04	0.13	0.03	0.44	–	0.07	0.09
FeO^t	0.14	0.16	0.00	0.07	–	0.13	0.27
MnO	0.01	0.02	0.01	0.03	–	0.02	0.02
MgO	0.07	0.05	0.03	0.09	–	0.05	0.19
CaO	0.04	0.14	0.01	0.20	–	0.04	0.09
Na_2O	0.14	0.07	0.01	0.12	–	0.05	0.06
K_2O	0.03	0.00	0.00	0.10	–	0.01	0.03
P_2O_5	0.02	0.03	0.02	0.04	–	0.02	0.02
Cl	0.00	0.00	0.00	0.00	–	0.01	0.00
SO_3^t	0.00	0.00	0.00	0.00	–	0.00	0.01
CIPW norm (wt%)							
q	0.00	12.72	0.62	3.51	9.34	1.57	1.54
hy	5.89	11.96	15.32	13.93	12.19	18.86	20.06
ol	6.10	0.00	0.00	0.00	0.00	0.00	0.00
S-K_α peak position							
$\%S^{+6}$	9	71	No peak	No peak	No peak	65	95
1σ	23	15	–	–	–	10	24
Olivine-corrected glass analysis							
Wt% olivine	2	2	2	3	3	0	0
SiO_2	53.42	60.43	54.89	56.57	59.22	55.14	54.58
TiO_2	1.19	1.78	1.12	1.32	1.61	1.09	1.09
Al_2O_3	19.12	14.76	17.78	16.22	15.13	17.65	17.66
FeO^t	7.18	6.89	7.65	7.84	7.17	7.83	8.21
MnO	0.12	0.11	0.16	0.13	0.14	0.12	0.14
MgO	4.69	4.06	4.80	4.96	4.52	5.00	5.19
CaO	7.77	5.35	7.13	6.35	5.48	7.18	7.38
Na_2O	4.56	4.10	4.31	4.44	4.36	4.12	3.93
K_2O	1.34	1.83	1.59	1.66	1.79	1.30	1.17
P_2O_5	0.33	0.53	0.31	0.34	0.45	0.31	0.33
Cl	0.09	0.10	0.10	0.09	0.10	0.09	0.09
SO_3^t	0.18	0.07	0.15	0.07	0.02	0.16	0.22
Total	99.99	99.99	99.99	99.99	99.99	100.00	100.00

Sample	116301-4B	116301-4D	116301-4E	116301-4F	116301-4H
No. spots	3	2	2	2	2
(wt%)					
SiO_2	56.92	56.82	56.79	56.32	55.77
TiO_2	0.80	0.86	0.87	0.95	0.80
Al_2O_3	17.63	18.66	18.58	19.20	16.99
FeO^t	6.88	5.33	5.87	6.53	7.10
MnO	0.08	0.07	0.15	0.11	0.12
MgO	3.65	1.33	2.28	3.31	4.27
CaO	6.76	7.14	7.83	6.88	6.20
Na_2O	3.92	3.93	4.11	4.41	2.96
K_2O	1.35	1.44	1.53	1.58	1.32
P_2O_5	0.25	0.28	0.26	0.27	0.30
Cl	0.10	0.10	0.09	0.10	0.08
SO_3^t	0.13	0.18	0.12	0.17	0.12
Total	98.47	96.14	98.50	99.82	96.04
1σ					
SiO_2	0.27	0.23	0.28	0.18	0.34
TiO_2	0.03	0.01	0.02	0.02	0.07
Al_2O_3	0.08	0.11	0.13	0.18	0.11
FeO^t	0.26	0.54	0.04	0.10	0.14
MnO	0.05	0.02	0.02	0.01	0.03
MgO	0.11	0.20	0.01	0.03	0.03
CaO	0.12	0.14	0.10	0.03	0.13
Na_2O	0.18	0.06	0.02	0.07	0.83
K_2O	0.04	0.04	0.02	0.02	0.03
P_2O_5	0.02	0.01	0.01	0.00	0.02

Table 4 (Contd.)

Sample	116301-4B	116301-4D	116301-4E	116301-4F	116301-4H
No. spots	3	2	2	2	2
Cl	0.00	0.00	0.01	0.00	0.01
SO_3^t	0.00	0.01	0.00	0.08	0.00
CIPW norm (wt%)					
q	7.09	10.52	6.48	3.11	10.94
hy	15.70	7.86	9.04	14.36	20.50
ol	0.00	0.00	0.00	0.00	0.00
S-K_α peak position					
$\%S^{+6}$	67	53	41	17	32
1σ	19	22	19	11	14
Olivine-corrected glass analysis					
Wt% olivine	1	5	3	1	0
SiO_2	57.61	58.14	57.09	56.25	58.07
TiO_2	0.80	0.85	0.86	0.94	0.84
Al_2O_3	17.73	18.44	18.30	19.04	17.69
FeO^t	7.10	6.15	6.33	6.66	7.39
MnO	0.08	0.08	0.15	0.11	0.13
MgO	4.10	3.41	3.52	3.70	4.45
CaO	6.80	7.06	7.71	6.82	6.45
Na_2O	3.94	3.88	4.05	4.37	3.09
K_2O	1.36	1.42	1.51	1.56	1.37
P_2O_5	0.25	0.28	0.26	0.27	0.32
Cl	0.10	0.10	0.09	0.09	0.09
SO_3^t	0.13	0.17	0.12	0.17	0.12
Total	100.00	100.00	99.99	100.00	100.00

glass compositions for the four studied samples. Three different analytical runs were conducted on each sample.

Glasses were analyzed for SiO_2, TiO_2, Al_2O_3, FeO^t, MnO, MgO, CaO, Na_2O, K_2O, P_2O_5, and Cl using a beam current of 10 nA and a 10 μm spot size. Smithsonian standards VG-2 glass, VG-A99 glass, VG-568 glass, Kakanui hornblende, manganite, Durango apatite, scapolite, and Johnstown hypersthene (Jarosewich et al. 1980) were used as primary standards to calibrate the instrument and as secondary, in-run standards to test for consistency. Between one and five separate spots were analyzed on each glass inclusion depending upon size; average and 1σ values are given in Table 4. Plagioclase microphenocrysts and microlites were analyzed under the same conditions. These data are discussed but not tabulated.

A second run was made to determine sulfur concentrations and the ratio of S^{6+} to S^{2-} in glasses by electron microprobe, following Carroll and Rutherford (1988), Nilsson and Peach (1993), Wallace and Carmichael (1994), Metrich and Clocchiatti (1996), and Matthews et al. (1999). In this study, the sulfur oxidation ratio is expressed as the percent $S^{6+}[= 100 \times S^{6+}/(S^{6+} + S^{2-})]$. Sulfur analyses were conducted using a PETH crystal (d = 4.371 Å), a beam current of 40 nA, and a 10 μm spot. The sulfur $K_{\alpha 1}$ peak position was first determined for each glass inclusion using a peak-search routine on three separate spots. The mean position was compared

Table 5 Electron microprobe analyses of Parícutin matrix glasses

Sample	108135		108139		108153		116301-4	
No. spots	12		10		9		11	
	Mean	1σ	Mean	1σ	Mean	1σ	Mean	1σ
(wt%)								
SiO_2	58.48	0.40	59.05	0.44	58.59	0.44	63.42	0.48
TiO_2	1.64	0.07	1.42	0.08	1.60	0.06	1.39	0.11
Al_2O_3	14.51	0.19	15.34	0.13	14.87	0.30	13.93	0.30
FeO^t	8.95	0.19	8.08	0.19	8.13	0.30	7.12	0.54
MnO	0.17	0.03	0.16	0.02	0.17	0.02	0.12	0.02
MgO	3.43	0.03	3.45	0.10	3.41	0.10	2.00	0.11
CaO	5.60	0.12	5.53	0.08	5.58	0.19	4.01	0.30
Na_2O	3.88	0.11	3.94	0.09	3.87	0.10	3.95	0.33
K_2O	1.45	0.05	1.67	0.05	1.88	0.09	2.33	0.31
P_2O_5	0.40	0.02	0.39	0.02	0.45	0.03	0.44	0.03
SO_3^t	0.009	0.005	0.009	0.005	0.009	0.004	0.010	0.003
Cl	0.10	0.01	0.09	0.01	0.08	0.01	0.07	0.01
Total	98.61	–	99.13	–	98.65	–	98.80	–

Table 6 Electron microprobe analyses of olivine adjacent to glass inclusions. Each analysis (*n* gives number of individual points) is listed in two lines: the average (first line) and 1σ values (second line)

Sample	*n*	SiO_2	Cr_2O_3	FeO	MnO	MgO	NiO	CaO	Total	Mg#
108135-A	5	40.62	0.03	15.23	0.22	45.51	0.36	0.15	102.11	84.2
		0.23	0.01	0.13	0.01	0.21	0.05	0.01		0.1
108135-B	3	38.70	0.00	14.64	0.19	44.50	0.33	0.14	98.51	84.4
		0.20	0.00	0.01	0.02	0.10	0.02	0.01		0.0
108135-C	5	39.82	0.02	15.11	0.21	44.84	0.38	0.14	100.53	84.1
		0.23	0.01	0.26	0.01	0.21	0.04	0.01		0.3
108135-D	3	38.97	0.05	15.06	0.22	44.66	0.36	0.15	99.47	84.1
		0.11	0.02	0.11	0.02	0.12	0.03	0.00		0.1
108139-A	4	39.59	0.02	16.10	0.24	43.52	0.25	0.16	99.89	82.8
		0.42	0.01	0.17	0.00	0.21	0.01	0.02		0.2
108139-E	3	40.26	0.02	16.68	0.23	43.36	0.32	0.14	101.02	82.3
		0.10	0.00	0.11	0.02	0.45	0.02	0.01		0.2
108139-G	5	40.22	0.02	15.92	0.24	44.82	0.30	0.15	101.67	83.4
		0.14	0.02	0.25	0.02	0.37	0.02	0.01		0.3
108139-J	4	39.66	0.03	15.85	0.24	44.26	0.39	0.14	100.57	83.3
		0.10	0.02	0.32	0.02	0.26	0.04	0.02		0.2
108153-A	3	39.41	0.01	15.93	0.25	43.41	0.29	0.17	99.47	82.9
		0.36	0.01	0.15	0.02	0.55	0.03	0.01		0.3
108153-C	3	39.31	0.01	15.95	0.24	43.93	0.32	0.14	99.90	83.1
		0.03	0.01	0.28	0.01	0.04	0.04	0.01		0.2
108153-D	3	39.32	0.01	15.92	0.24	43.79	0.33	0.14	99.74	83.1
		0.06	0.00	0.25	0.01	0.08	0.01	0.01		0.2
108153-F	3	39.68	0.02	15.72	0.22	44.69	0.36	0.15	100.85	83.5
		0.10	0.01	0.24	0.01	0.18	0.04	0.01		0.2
108153-H	3	39.28	0.04	16.24	0.24	44.15	0.33	0.14	100.43	82.9
		0.05	0.01	0.12	0.01	0.25	0.04	0.01		0.2
108153-I	3	39.34	0.01	16.24	0.24	43.94	0.28	0.14	100.19	82.8
		0.11	0.01	0.11	0.00	0.02	0.02	0.02		0.1
108153-J	3	39.19	0.01	17.48	0.27	43.29	0.25	0.16	100.65	81.5
		0.19	0.01	0.80	0.04	0.81	0.02	0.02		1.0
108153-K	3	39.02	0.03	16.34	0.24	43.29	0.29	0.14	99.35	82.5
		0.12	0.01	0.22	0.01	0.24	0.02	0.02		0.2
108153-La	3	39.34	0.00	16.70	0.24	43.64	0.24	0.15	100.31	82.3
		0.06	0.00	0.04	0.01	0.17	0.02	0.01		0.1
108153-Lb	3	39.40	0.02	16.69	0.24	44.23	0.26	0.15	101.00	82.5
		0.05	0.01	0.20	0.01	0.15	0.03	0.02		0.2
116301-4B	4	37.86	0.02	17.86	0.26	41.71	0.27	0.14	98.12	80.6
		0.04	0.01	0.16	0.01	0.17	0.02	0.01		0.2
116301-4D	3	38.15	0.02	17.28	0.25	40.50	0.35	0.12	96.67	80.7
		0.08	0.00	0.10	0.02	0.03	0.04	0.01		0.1
116301-4E	3	39.15	0.01	18.58	0.25	42.74	0.26	0.13	101.13	80.4
		0.10	0.01	0.05	0.00	0.04	0.03	0.02		0.0
116301-4F	3	38.79	0.01	18.48	0.26	41.58	0.26	0.14	99.54	80.0
		0.14	0.01	0.08	0.02	0.12	0.05	0.02		0.1
116301-4H	3	38.88	0.01	18.51	0.27	42.17	0.27	0.13	100.24	80.2
		0.12	0.01	0.12	0.02	0.18	0.03	0.01		0.0

with the mean positions for five different spots measured on standards of troilite (pure S^{2-}) and anhydrite (pure S^{6+}) to establish the percent S^{6+}. The difference between the troilite and anhydrite peaks was typically 1.35 eV, and the average 1σ uncertainty on the sulfur $K_{\alpha 1}$ peak position on glass was 0.23 eV, equivalent to a 1σ uncertainty of 17% on the percent S^{6+} value, although these uncertainties ranged broadly in inverse relation to the amount of sulfur present. Table 4 lists percent S^{6+} and 1σ values for each glass inclusion. Sulfur concentration data were taken at the peak position established for each inclusion, using the Smithsonian scapolite with 1.32 wt% SO_3^t (Jarosewich et al. 1980) as the primary standard, measured at its determined peak position for 80 s. Three different spots were typically measured on each glass inclusion, with averages and 1σ values listed in Table 4. Standard glass 620 (NIST 1995: 0.28 wt% SO_3^t) was used as an in-run sulfur standard to test for consistency.

A third run measured the composition of olivine immediately adjacent to the glass inclusion. These analyses were conducted using a beam current of 20 nA and a focused spot. Smithsonian standards San Carlos olivine, Springwater olivine, synthetic forsterite, Kakanui hornblende, and Johnstown hypersthene (Jarosewich et al. 1980) were used as primary standards to calibrate the instrument and as secondary, in-run standards to test for consistency. Between three and five spots were measured on olivine at different points along the inclusion margin, each centered ~5 μm from the glass contact; average and 1σ values are given in Table 6. Olivine and orthopyroxene (sample 116301-4) microphenocrysts

Table 7 Fourier transform infrared spectroscopic data for H_2O in Parícutin glass inclusions. Species abundances were calculated from the Beer–Lambert Law: $c_i = (18.02A_i)/(d\rho\epsilon_i)$, where c_i is the concentration of species i expressed as a weight fraction, 18.02 is the molecular weight of water, A_i is the height of the absorbance peak, d is the thickness of the specimen in cm, ρ is the density of the glass in g/l, and ϵ_i is the molar absorptivity in l/mol-cm

	Thickness (μm)	Density (g/l)	Molecular H_2O 1,635 cm^{-1}		Molecular H_2O 5,200 cm^{-1}		OH 4,500 cm^{-1}		OH Δ mid-IR[a] H_2O (wt%)	Total H_2O near-IR[b] H_2O (wt%)	Total H_2O 3,535 cm^{-1}		H_2O Saturation at 1,100 °C (bar)[c]
			Abs.	H_2O (wt%)	Abs.	H_2O (wt%)	Abs.	H_2O (wt%)			Abs.	H_2O (wt%)	
108135-A	35	2,549	0.362	2.1	–	–	–	–	1.9	–	1.247	4.0	1,380
108135-B	46	2,585	0.351	1.5	0.0106	1.6	0.0075	1.4	1.5	3.0	1.275	3.1	875
108135-C	60	2,609	0.305	1.0	0.0080	0.9	0.0090	1.2	1.5	2.1	1.371	2.5	600
108135-D	30	2,602	0.118	0.8	0.0050	1.1	0.0073	2.0	1.9	3.1	0.737	2.7	685
108139-A	76	2,546	0.555	1.5	0.0150	1.4	0.0220	2.5	–	3.9	–	–	1,310
108139-G	44	2,571	0.328	1.5	–	–	–	–	1.3	–	1.113	2.8	728
108139-J1	62	2,605	0.251	0.8	–	–	–	–	1.0	–	1.009	1.8	340
108139-J2	62	2,598	0.166	0.5	–	–	–	–	1.4	–	1.087	1.9	375
108153-A	60	2,533	0.510	1.8	0.0140	1.6	0.0170	2.4	–	4.0	–	–	1,375
108153-La	51	2,602	0.140	0.6	–	–	–	–	1.3	1.1	0.874	1.9	372
116301-4B	51	2,534	0.351	1.4	0.0100	1.4	0.0090	1.5	1.4	2.9	1.283	2.8	735
116301-4D	17	2,484	0.131	1.6	–	–	–	–	1.5	–	0.468	3.2	940
116301-4H	58	2,551	0.240	0.8	0.0080	0.9	0.0100	1.5	1.3	2.4	1.117	2.2	485

[a]OH Δ mid-IR is calculated from mid-IR data by subtracting molecular H_2O (1,635 cm^{-1}) from total H_2O (3,535 cm^{-1}) and is listed for comparison with OH measured from the near-IR peak at 4,500 cm^{-1}

[b]Total H_2O near-IR is the sum of molecular H_2O (5,200 cm^{-1}) and OH (4,500 cm^{-1}) and is listed for comparison with total H_2O calculated from the mid-IR peak at 3,535 cm^{-1}

[c]H_2O-saturation pressures were calculated at 1,100 °C from the estimates for Total H_2O and glass compositions in Table 4 using the model of Moore et al. (1998)

and microlites were analyzed under the same conditions. These data are discussed but not tabulated.

Fourier transform infrared spectroscopy

Of the 26 glass inclusions analyzed by electron microprobe, only half were suitable for analysis by transmission FTIR spectroscopy. FTIR spectra were obtained in the mid-infrared (mid-IR: 400–4,000 cm^{-1}) and near-infrared (near-IR: 3,000–8,000 cm^{-1}) regions using a Bio-Rad MA-500 microscope attached to a Bio-Rad Excalibur FTIR spectrometer. The microscope was equipped with an MCT detector cooled with liquid nitrogen. A KBr beam splitter was used in the bench for all analyses. The mid-IR spectra were taken with a ceramic (Permaglow) source, whereas near-IR spectra were taken with a tungsten–halogen source. The bench and microscope were continuously purged with air from which the water and carbon dioxide had been removed using a Whatman purge-gas generator, in order to minimize interference with components in the atmosphere. Thicknesses of the doubly polished wafers were measured by adhering each wafer edge to a needle, rotating it under a binocular microscope so the wafer was vertical, and measuring the inclusion thickness against the microscope reticle (Table 7). The precision of this method, determined by repeated measurements, is ~3 μm (1σ).

All glass inclusions were first analyzed for H species in the mid-IR (Table 7). Total water (molecular H_2O plus OH^-) was evaluated from the broad asymmetric peak at 3,535 cm^{-1}, which is interpreted as the fundamental OH^- stretching vibration (Scholze 1959; Nakamoto 1978; Stolper 1982). A molar absorptivity of 63 ± 3 l/mol-cm is assumed for the 3,535 cm^{-1} peak in this study (Dobson, Newman, Epstein, and Stolper, unpublished; cited in Dixon et al. 1995). The baseline was drawn as a straight line using Bio-Rad software, and peak height was measured at 3,535 cm^{-1}. Molecular H_2O was evaluated from the peak at 1,635 cm^{-1}, which is interpreted as a symmetrical bending mode (Nakamoto 1978). Baselines were drawn by hand with a flexicurve. A molar absorptivity was calculated for the 1,635 cm^{-1} peak from the following equation fit to data in Fig. 2 of Dixon et al. (1995): $e^{1635} = -66.3 + 141.7 \times T$, where T is Si + Al/total cations as defined by Dixon et al. (1995). The average molar absorptivity calculated for Parícutin glasses, 34.5 ± 2.1 (1σ), was used for calculation of all concentrations of molecular H_2O from the 1,635 cm^{-1} peak.

Most of the Parícutin glass inclusions have relatively high water contents that cause absorbance values for the 3,535 cm^{-1} peaks to exceed 0.8 (Table 7). An absorbance of 0.8 indicates that the transmitted beam intensity has fallen to 15% of the incident beam intensity, and is commonly taken as a limit of validity for calculation of species abundance from the Beer–Lambert Law (Ihinger et al. 1994; Smith 1996). Absorbance values up to 1.4 (= 4% transmission) are listed in Table 7. In most of these cases, the significantly less sensitive peaks in the near-IR region were also utilized: the 5,200 cm^{-1} peak for molecular H_2O (stretching plus bending mode: Scholze 1960; Bartholomew et al. 1980; Stolper 1982)

Table 8 Fourier transform infrared spectroscopic data for CO_3^{2-} in Parícutin glass inclusions. CO_2 abundances were calculated as discussed in Table 7, except that 44.01 was taken as the molecular weight of CO_2, and a molar absorptivity of 279 was used (see text)

	Thickness (μm)	Density (g/l)	CO_3^{2-} 1,515 cm^{-1}		CO_3^{2-} 1,435 cm^{-1}		CO_2	
			Abs.	CO_2 (ppm)	Abs.	CO_2 (ppm)	Avg. (ppm)	1σ (ppm)
108135-A	35	2,549	0.016	283	0.012	212	248	35
108153-A	60	2,533	0.018	187	0.039	405	296	109

and the 4,500 cm^{-1} peak for OH^- (stretching plus bending modes of Si–OH groups, with a possible additional contribution from Al–OH groups: see Stolper 1982). Baselines were drawn by hand with a flexicurve. Molar absorptivities were calculated from the regression equations reported in Dixon et al. (1995): $\epsilon^{5200} = -2.6 + 5.1 \times T$, and $\epsilon^{4500} = -2.3 + 4.4 \times T$, where T is defined as explained above. Average values calculated for the Parícutin glasses were used in all cases: 0.83 ± 0.07 (1σ) for OH^- at 4,500 cm^{-1}, and 1.03 ± 0.08 (1σ) for molecular H_2O at 5,200 cm^{-1}. Despite absorbance values up to 1.4, total H_2O values calculated from the 3,535 cm^{-1} peaks are not systematically different from total H_2O values calculated from the sum of the 5,200 cm^{-1} peak and the 4,500 cm^{-1} peak (Table 7). These results indicate that an absorbance limit of 0.8 for application of the Beer–Lambert law may be too conservative.

Only two of the 13 analyzed glass inclusions had detectable peaks at the 1,515 cm^{-1} and 1,435 cm^{-1} positions, corresponding to antisymmetric stretching of distorted carbonate (CO_3^{2-}) groups (Fine and Stolper 1986). No samples showed a detectable peak at the 2,350 cm^{-1} position for the antisymmetric stretching mode of molecular CO_2 (Fine and Stolper 1985). A molar absorptivity of 279 ± 11 l/mol-cm was calculated for the 1,515 cm^{-1} and 1,435 cm^{-1} peaks from the correlation with molar Na/(Na + Ca) derived by Dixon and Pan (1995), using the average Na/(Na + Ca) value for Parícutin glass inclusions, 0.50 ± 0.03 (1σ). The infrared spectrum for a dehydrated and decarbonated glass prepared in a 1 atm furnace at 1,200 °C from a powdered Parícutin scoria sample (116301-3) was used as a reference to compensate for the considerable background complexity in this spectral region. A Bio-Rad software routine was used to perform point-by-point subtraction of the absorbance values in the reference spectrum from those in each measured sample spectrum. A straight background was then drawn by hand and peak height was measured graphically. Results are given in Table 8.

Glass densities, necessary for calculation of the abundances of chemical species from FTIR data, are listed in Table 7. They were calculated from a simple summation of molecular partial molar volume contributions using the following parameters (R. Lange, personal communication 1999; based on density measurements for a wide compositional range of glasses at 1 bar and 25 °C): $SiO_2 = 27.01 \pm 0.11$ (cm^3/mol), $Al_2O_3 = 37.76 \pm 0.38$, FeO = 10.5 (preliminary), MgO = 8.81 ± 0.26, CaO = 13.03 ± 0.26, $Na_2O = 19.88 \pm 0.29$, $K_2O = 33.63 \pm 0.49$, and $H_2O = 13.93 \pm 0.30$. Glass densities calculated according to this model (TiO_2, Fe_2O_3, MnO, and P_2O_5 were not considered; H_2O was calculated iteratively) are thought to have a 1σ error of 0.5%, equivalent to about 130 g/l for a typical density of 2,600 g/l.

Considering the typical 1σ uncertainties on the various terms in the Beer–Lambert Law (absorbance measurement ~5%, glass density ~0.5%, wafer thickness ~6%, and molar absorptivity ~6%) the 1σ uncertainties on individual FTIR measurements are estimated as ~10%. The detection limit for carbonate in the Parícutin glasses is estimated as ~50 ppm equivalent CO_2.

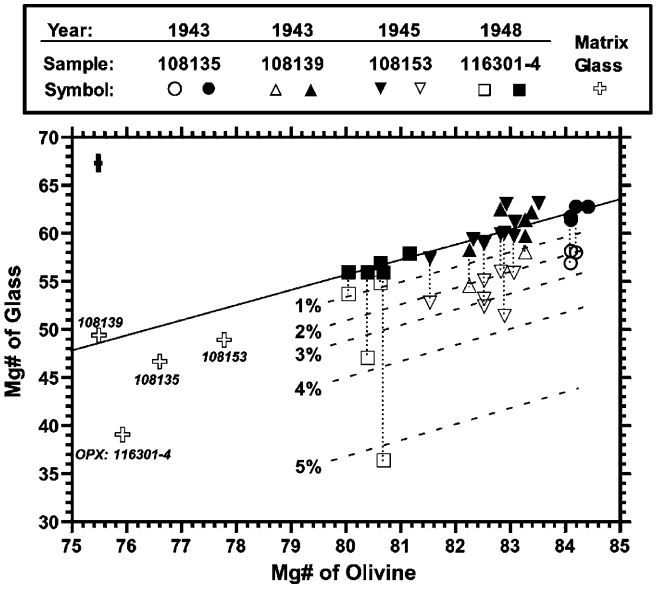

Fig. 6 Mg# in adjacent olivine [100×Mg/(Mg + Fe^t)] versus Mg# in glass {100×Mg/[Mg + (0.78×Fe^t)]}, assuming that 22 at% of the Fe^t is Fe^{3+}. Raw data are shown as *open symbols*. The *solid sloping line* shows the experimentally determined partitioning relationship for Fe^{2+} and Mg between olivine and silicate melt (Ulmer 1989). *Solid symbols* connected by *vertical dotted tie-lines* to the raw data are glass compositions that have been corrected by incrementally adding 1 wt% host olivine back into the glass composition until the equilibrium relationship is achieved. *Dashed lines* labeled 1 to 5% approximately show the wt% of olivine necessary to add to the glass composition to reach equilibrium partitioning. The four *open crosses* at low olivine Mg# represent compositions of matrix glasses (Table 5) and olivine microphenocrysts, with the exception of sample 116301-4, where orthopyroxene microphenocryst compositions were used because no olivine microphenocrysts are present. *Error bars* reflect 1σ counting statistics for electron microprobe analyses

Discussion

Mineral compositions

Wilcox (1954) discussed the compositions of Parícutin minerals based on optical measurements. His interpretations for olivine and orthopyroxene were confirmed by electron microprobe analyses presented in Bannister et al. (1998). The latter authors pointed out, however, that the "titanomagnetite" inclusions in olivine described by Wilcox (1954) are actually chromite.

Bannister et al. (1998) described olivine phenocrysts erupted from Parícutin in 1943–1947 as having core compositions of $Fo_{80–84}$ with rims zoned to Fo_{75}. In this study, olivine core compositions (Table 6) were measured adjacent to the analyzed glass inclusions. Average Fo values of these olivine cores decreased systematically with eruption date: 108135 (1943), $Fo_{84.2 \pm 0.1}$; 108139 (1943), $Fo_{82.9 \pm 0.5}$; 108153 (1945), $Fo_{82.7 \pm 0.5}$; 116301-4 (1948), $Fo_{80.4 \pm 0.2}$. Olivine phenocryst rims, microphenocrysts, and matrix microlites in all four samples range down to $Fo_{75–78}$, also consistent with the data of Bannister et al. (1998) on Parícutin lavas. Cores of Parícutin orthopyroxene phenocrysts range $En_{80–82}$ (Bannister et al. 1998). The orthopyroxene microphenocrysts and matrix crystals analyzed in this study are more Fe-rich at $En_{76.6 \pm 1.5}$. No electron microprobe analyses of plagioclase in Parícutin rocks have been published previously. The microphenocrysts and microlites analyzed in this study range $An_{56–61}$, with no systematic change over time.

Glass inclusion compositions and corrections for olivine precipitation

Post-entrapment crystallization of melt inclusions onto the walls of the host crystal is likely to occur during eruptive cooling, and can significantly deplete the melt for elements that are strongly enriched in the host crystal, such as Mg in olivine. Electron microprobe traverses across the crystal inclusion boundary are unlikely to identify such post-entrapment growth zones until high degrees of crystallization are reached. For example, more than 10% crystallization of an inclusion 50 μm in diameter will leave a new mineral shell only 1 μm wide. Experimentally determined partitioning relationships for Fe–Mg between olivine and melt (Ulmer 1989) can be used to sensitively monitor such precipitation. Fig. 6 is a plot of Mg# in adjacent olivine versus Mg# in glass inclusions. Many (16 of 26) of the analyzed glass compositions (open squares, triangles, circles) fall below the equilibrium line and are interpreted to have undergone up to 5 wt% loss of olivine. These analyses were corrected (solid symbols) by iteratively adding 1 wt% of the host olivine composition to the glass composition, and then evaluating the Fe–Mg partitioning against the equilibrium relationship of Ulmer (1989). Most analyses converged on approximately equilibrium values after just 1–3 wt% olivine addition, with 5% being the highest required. A few inclusions fall above the equilibrium line; these analyses have not been corrected. The olivine-corrected analyses are also listed in Table 4 and used in all subsequent discussion. Also shown on the left side of Fig. 6 are compositional pairs of matrix glasses (Table 5) and olivine or orthopyroxene (sample 116301-4) microphenocrysts and microlites. The three olivine-based pairs conform reasonably well to the equilibrium line, whereas the orthopyroxene-based pair falls well below the line, indicating that the olivine–melt equilibrium relationships do not perfectly match those for orthopyroxene–melt.

Compositional variations in glasses and whole-rock samples

Bulk-scoria/ash and glass compositions from this study are plotted along with published whole-rock lava samples from the Parícutin eruption in Fig. 7. Largely based on the volume-SiO_2 and -K_2O trends of Fig. 7a and c, the eruption is divided into three stages, with boundaries at 20 and 70% erupted. The stage-1 volume-K_2O trend is essentially flat, and all samples have lower K_2O than those for stage 2. The stage-2 volume-K_2O trend has a slight positive slope, and that for stage 3 a significantly steeper slope. The four studied scoria/ash samples (large solid symbols in Fig. 7) conform well to the whole-rock lava trends and help to close some of the temporal gaps with no lava data. They span the three eruption stages, representing 15 to 84% of the vol% erupted.

Harker diagrams depicting compositional variations of whole-rock and glass samples versus SiO_2 are presented in Fig. 8. Although many of the bulk-scoria/ash and glass analyses from this study conform to the whole-rock lava trends, some important differences are evident. Tie-lines join the four bulk-scoria/ash samples to their respective matrix glasses. The tie-line trends for TiO_2, P_2O_5, and Al_2O_3 versus SiO_2 diverge steeply from the main lava trends. Since these tie-lines reflect the crystallization of olivine and plagioclase in the scoria/ash samples (plus orthopyroxene in the case of 116301-4), they provide strong evidence that crystallization of these minerals alone can not explain the compositional trends of Parícutin's lavas. Wilcox (1954) and McBirney et al. (1987) made the same observation and argued that assimilation of crustal granitic rocks accompanied crystallization of olivine, plagioclase, and orthopyroxene. The granitic xenoliths from Parícutin and nearby outcrops show wide compositional variations. A simple mixing line between the average granitic composition and scoria sample 108135 is shown on Fig. 8, offering support to the interpretation of Wilcox (1954) and McBirney et al. (1987).

The earliest of the scoria samples (108135) is slightly poorer in SiO_2 than any analyzed lava sample. Nine of the 26 analyzed glass inclusions have even lower SiO_2

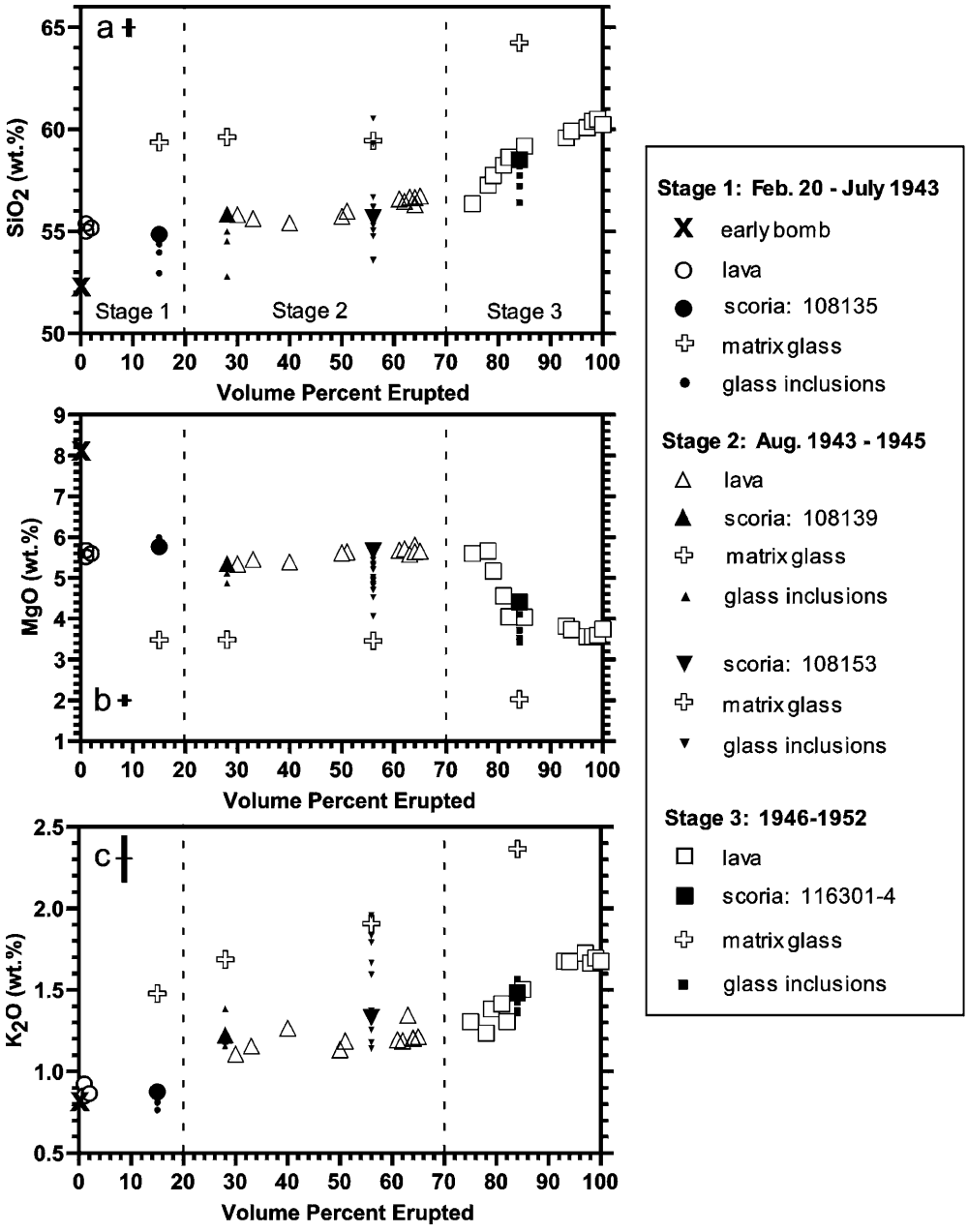

Fig. 7 Volume percent erupted, taken from Fig. 2 of McBirney et al. (1987) after Fries (1953), versus whole-rock and glass values of SiO_2 **a**, MgO **b**, and K_2O **c**. Data include whole-rock lava samples (*open circles*, *diamonds*, and *squares*: Wilcox 1954; McBirney et al. 1987), bulk-scoria/ash samples (*large closed symbols*: Table 3), glass inclusions (*small closed symbols*: Table 4), matrix glasses (*open crosses*: Table 5), and the early bomb of Anguiano and Martínez (*x*: unpublished data). All analyses have been normalized similarly, with all Fe as FeO and with the sum of SiO_2, TiO_2, Al_2O_3, FeO^t, MnO, MgO, CaO, Na_2O, K_2O, and P_2O_5 equal to 100%. The eruption has been divided into three stages, with break points at 20 and 70% erupted. *Error bars* for element values reflect 1σ counting statistics for electron microprobe analyses of glass inclusions. These errors are larger than those for whole-rock analyses by XRF or wet chemistry

contents, ranging to below 53 wt%. These mafic glasses are found in olivines ($Fo_{82.2–84.4}$) from the three earliest scoriae, erupted in 1943 and 1945, but are absent in the scoriae from 1948. They provide evidence for melts that are parental to the main Parícutin lava suite. Another intriguing sample with regard to evaluating the parental magma of the Parícutin suite is a bomb collected while still hot on February 20, 1943, in the first hours of the eruption, by two local men (Jesús Anguiano and Jesús Martínez) sent as part of delegation by the priest and municipal president of San Juan Parangaricutiro to investigate "smoke" rising to the south of the town (Foshag and González-Reyna 1956; Luhr and Simkin 1993). This early bomb is vesicular, unaltered, has a glassy rind, and contains ~4 vol% phenocrysts of both olivine (plus spinel inclusions) and plagioclase, an assemblage characteristic of only the earliest Parícutin samples; plagioclase phenocrysts were rare in lavas erupted after early 1944. This early bomb is shown by an "x" on Figs. 7 and 8. It has lower SiO_2 (52.3 wt%) and higher MgO and CaO than any other Parícutin sample: lava, scoria, or glass. Luhr and Housh (1993) presented elemental and isotopic data for this early bomb that were largely supportive of a parental relationship to the Parícutin suite, although a few inconsistencies exist. Foshag and González-Reyna (1956) dismissed the early bomb as an accidental lithic fragment, and it was not included in the study of McBirney et al. (1987).

Four small glass inclusions in $Fo_{81.5–82.9}$ olivine from sample 108153, erupted in 1945, diverge from the main compositional trends of the lavas, bulk-scoria/ash sam-

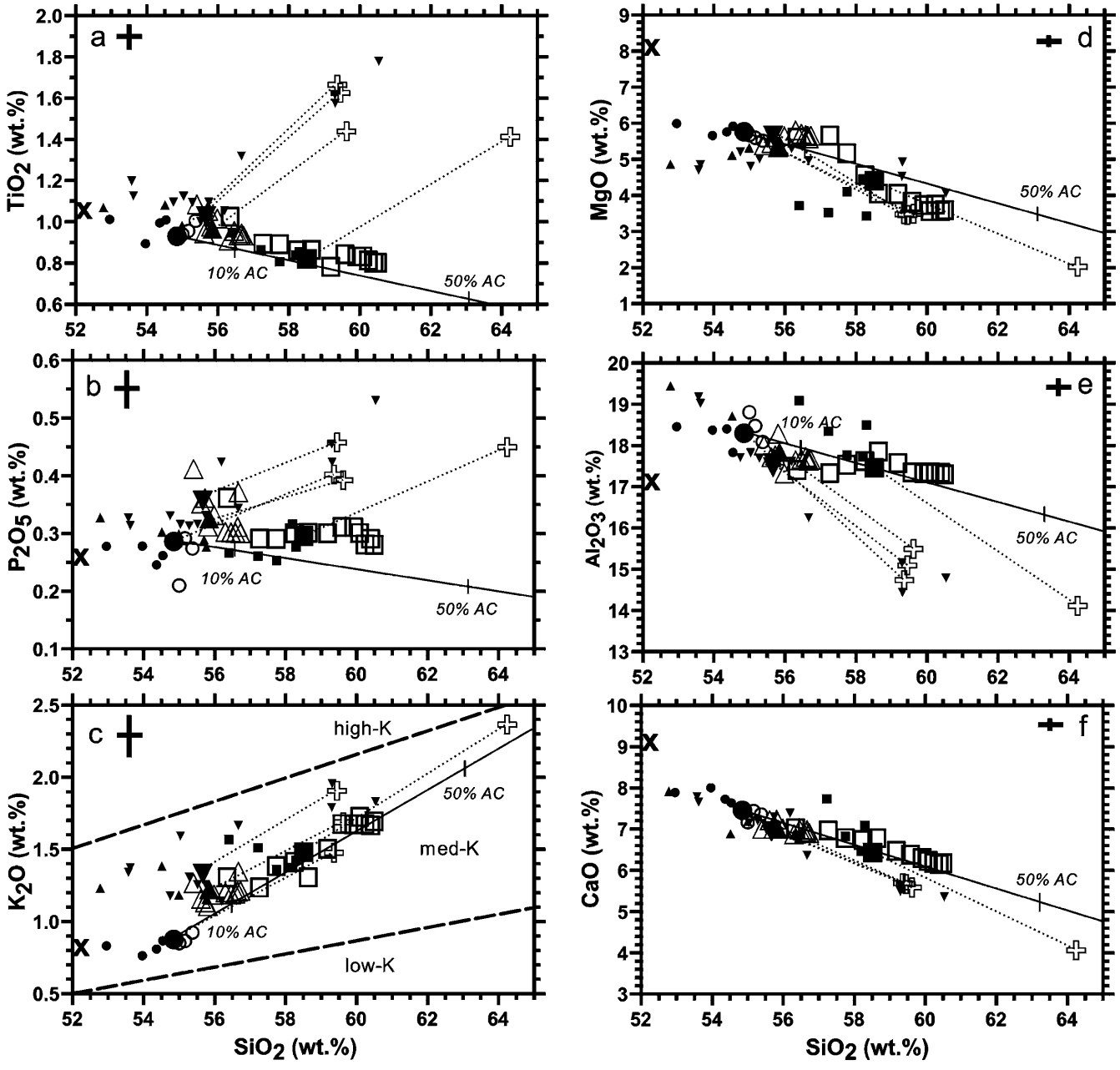

Fig. 8 Harker diagrams showing compositional variations of SiO_2 versus TiO_2 **a**, P_2O_5 **b**, K_2O **c**, MgO **d**, Al_2O_3 **e**, and CaO **f**. Data sources, symbols, normalization, and error bars as for Fig. 7. *Dotted lines* connect the bulk-scoria/ash samples to their respective matrix glasses. The *solid line* is a mixing trend between bulk-scoria sample 108135 and the average of 15 granitic basement rocks and inclusions from the Parícutin (Wilcox 1954; McBirney et al. 1987) and Jorullo areas (Luhr and Carmichael 1985). Two *tick marks* indicate 10 and 50% addition of average crust (*AC*)

ples, and other glass inclusions. These four glasses show strong positive correlations of TiO_2 and P_2O_5 versus SiO_2, and are comparatively depleted in both Al_2O_3 and CaO (Fig. 8). They conform to the dotted trend lines between bulk-scoria/ash samples and their matrix glasses, which confirms that they were generated by simple fractional crystallization of olivine plus plagioclase, without significant involvement of crustal assimilation. Unfortunately, none of these four glass inclusions are sufficiently large for FTIR analysis.

The Parícutin glasses show a wide variation of K_2O values at a given SiO_2 content; particularly at low SiO_2 levels, K_2O ranges nearly by a factor of two (Fig. 8c). Importantly, this variation shows considerable temporal dependence. A value of 1 wt% K_2O separates all stage-1 (pre-July, 1943) lavas, scoriae, and glasses (< 1 wt% K_2O) from all stage-2 and -3 (post-July, 1943) samples (> 1 wt% K_2O). Thus, long before the rather abrupt compositional transition in 1947 that McBirney et al. (1987) interpreted to reflect enhanced crustal contamination, discrete magma batches were erupted at Parícutin. The involvement of distinct magma types during single cinder cone eruptions have been reported previously. The 1975–1976 Tolbachik

fissure eruption in Kamchatka formed four new cinder cones and associated lava fields and involved an abrupt shift from one basaltic composition to another in September 1975 (Fedotov et al. 1991). An even closer analog to Parícutin is the ~2,000 year old basaltic eruption of Xitle volcano (Siebe 2000), south of Mexico City (Fig. 1). Cervantes and Wallace (2001) also documented the presence of two distinct magma types in the Xitle eruption. Many petrological studies in the MVB have emphasized the extreme diversity of magma types erupted contempora- neously from nearby vents (Luhr and Carmichael 1985; Luhr et al. 1989; Lange and Carmichael 1990, 1991; Wallace and Carmichael 1992; Wallace et al. 1992; Luhr 1997).

Volatile abundances in Parícutin magmas

In this study, the following volatile components were investigated in the Parícutin glass inclusions: H_2O (molecular), OH (hydroxyl), H_2O^t (combined molecular and hydroxyl), CO_3^{2-} (carbonate), Cl, and SO_3^t (total sulfur as SO_3).

Previous observations on Parícutin volatiles

Earlier studies of the Parícutin eruption aimed at constraining magmatic volatile abundances and temperatures included field-based observations and measure- ments, phase-equilibrium laboratory experiments, and electron microprobe analyses of glass inclusions. These data need to be reconciled with the analyses of gas species in glass inclusions presented in this study.

Throughout its 9 year life, most of the gaseous emissions accompanied tephra ejected from the central vent, whereas virtually all of the lava issued from flank vents at the SW and NE bases of the cinder cone. Foshag (1943) and Hernández-Velasco (1943) presented analyses of gases emitted from fumaroles along the margins of early lava flows. These were dominated by water and hydrochloric acid. Field observations reported in Foshag and González-Reyna (1956) emphasized light-purple to light-blue flames, whose edges were tinged with yellow, being emitted with the hissing sound of a blowtorch from hornitos and other orifices in lava flows, especially near the lava vents at the SW base (Plate 3A, Luhr and Simkin 1993). These flames were typically associated with a strong odor of hydrochloric acid. Krauskopf (1948a) noted that only traces of sulfur gases accompanied these emissions of hydrochloric acid at the lava vents, whereas sulfur was an important part of the dominantly steam emissions from the main crater.

Maximum temperatures for Parícutin lavas measured in the field by thermocouple and optical pyrometer decreased with time from 1,110 °C in December 1944 (Zies 1946), to 1,070 °C in late 1945 to early 1946 (Krauskopf 1948b), to 1,040 °C in October–November 1946 (Wilcox 1954).

Eggler (1972) conducted phase-equilibrium experiments on a Parícutin andesite from the last stages of the eruption (February 25, 1952). By comparing the phase assemblages and compositions in the natural rock (orthopyroxene, olivine, plagioclase) with those in experimental charges produced under varying temperature, pressure, and melt water contents, he concluded that the late-stage Parícutin magma had 2.2 ± 0.5 wt% H_2O in the melt at a temperature of $1{,}110 \pm 40$ °C.

Anderson (1973) presented electron microprobe analyses of six glass inclusions in $Fo_{81–82}$ olivine from a Parícutin ash sample erupted at some unspecified time prior to its collection on 6 March 1948. Based on the "difference method" and normalization to anhydrous basaltic glass from Kilauea Iki, Anderson concluded that the glass inclusions contained 0.1–1.7 wt% H_2O. If the electron microprobe totals are instead subtracted from 100% without referencing to the Kilauea Iki glass, the "difference method" indicates 2.1–3.6 wt% H_2O, consistent with the results of this study.

Hydrogen species: molecular water and hydroxyl

Values of molecular H_2O and hydroxyl for Parícutin glass inclusions, taken from Table 7, straddle the experimental speciation curves for mid-ocean ridge basalt glasses at 1,200 °C (Dixon et al. 1995). Because partitioning between molecular H_2O and hydroxyl is known to be dependent on quench rate (Zhang et al. 2000), this agreement supports the inference that the Parícutin inclusions quenched rapidly, which in turn is consistent with the evidence for relatively limited crystallization of olivine after entrapment. Thus, the Parícutin data appear to reflect high-temperature magmatic partitioning of hydrogen.

Total water contents for the glass inclusions range considerably (1.8–4.0 wt%) within a single sample, and show no systematic changes with either eruption date, host olivine Mg#, or SiO_2 content of the glass inclusion (Fig. 9a). Wide variations in total water contents of glass inclusions have been reported in other studies (Johnson et al. 1994; Cioni 2000; Cervantes and Wallace 2001). Possible explanations include fracturing and leakage of melt and volatiles from some inclusions, or volatile enrichments related to variable post-entrapment crystallization of the host mineral. The inclusion selection criteria employed in this study were designed to avoid inclusions that may have leaked. Furthermore, post-entrapment crystallization of olivine appears to have been minimal (Fig. 6). Thus, the range of total water contents is interpreted as a real reflection of variations in melt volatile contents beneath Parícutin. As the magmas ascended from depth, water and other volatiles would steadily bubble out of the melt to maintain the progressively reduced saturation limits. Olivine was probably precipitating over a wide range of upper crustal

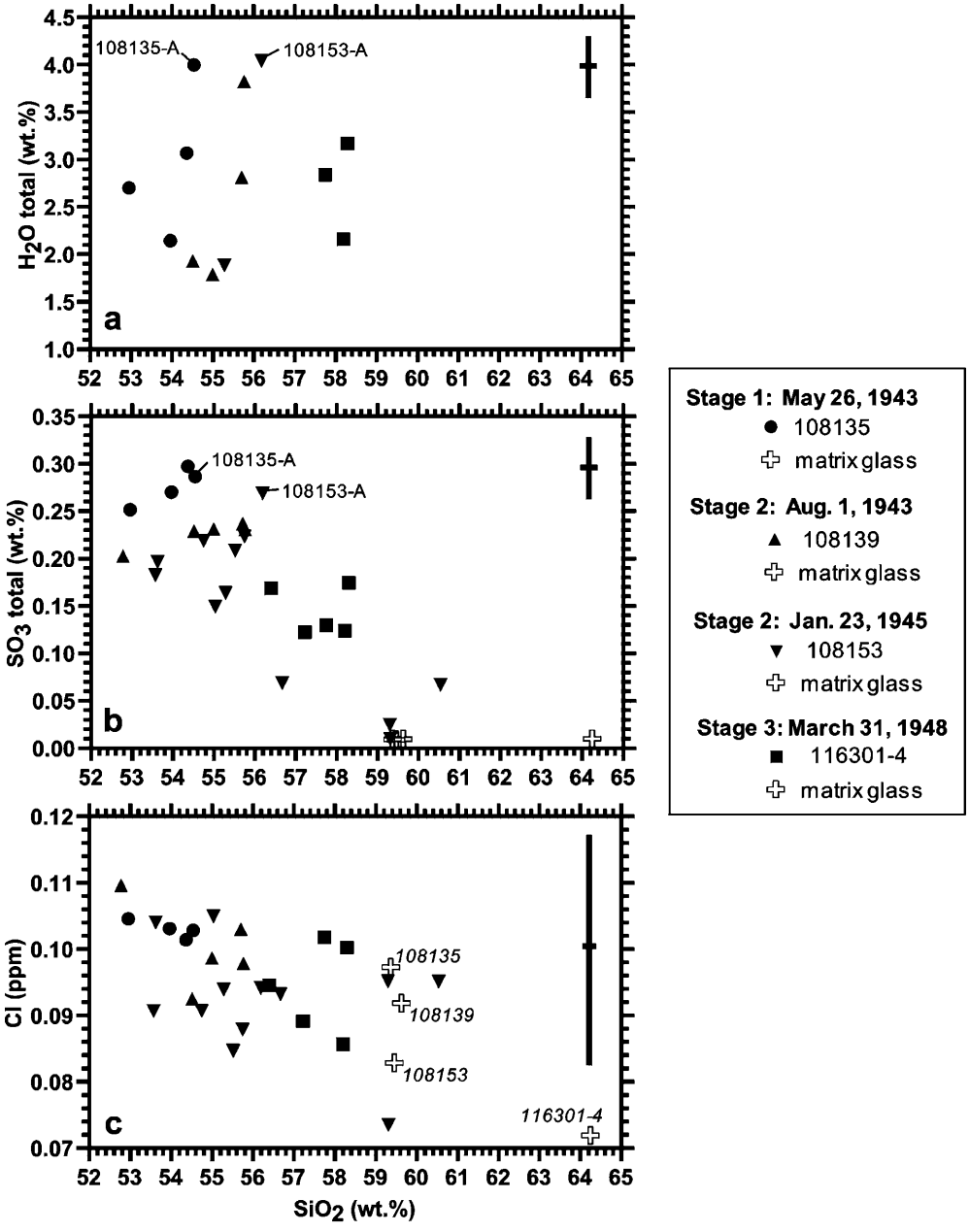

Fig. 9 Harker diagrams showing compositional variations of SiO_2 versus H_2O total **a**, SO_3 total **b**, and Cl **c** in Parícutin glass inclusions and matrix glasses. SiO_2 values have been normalized as described in Fig. 7 for consistency with that and other plots. All but two of the H_2O total values are those derived from the 3,535 cm^{-1} peak (Table 7). These two exceptions are inclusions 108139-A and 108153-A, for which the 3,535 cm^{-1} absorbance values were too high to apply the Beer–Lambert Law; for these samples total H_2O values are the summation of molecular H_2O values and OH values derived from the near-IR peaks at 5,200 and 4,500 cm^{-1}, respectively (Table 7). Values of total sulfur as SO_3 and Cl are as listed in Table 4, normalized and corrected for olivine crystallization to a 12-element total of 100%. The matrix glass analyses from Table 5 have been similarly normalized. *Error bars* for SiO_2, $SO_3{}^t$, and Cl as in Fig. 7. *Error bar* for H_2O total depicts estimated 1σ values of ~10%

depths in the vapor-saturated magmas beneath the volcano. Higher melt water contents probably record inclusions trapped at greater depths, and lower melt water contents record inclusions trapped at shallower levels. Mixing of magmas that trapped inclusions at these different depths could occur during ascent or during eruption (Spera 1984), to produce a single tephra horizon containing glass inclusions with widely varying total water contents.

The range of total water contents in Parícutin glass inclusions (1.8–4.0 wt%) brackets the estimate by Eggler (1972) of 2.2 ± 0.5 wt% H_2O based on phase-equilibrium experiments to duplicate the mineral assemblage of a 1952 Parícutin andesite. Moore and Carmichael (1998) conducted similar experiments on an andesite and a basaltic andesite from western Mexico, compositions that closely bracket the whole-rock compositional range for the Parícutin eruption. The basaltic–andesite phase diagram (their Fig. 4) indicates that the pre-eruptive assemblage in the early Parícutin basaltic andesites (olivine + chromite + plagioclase + melt), relevant to the samples erupted in 1943–1944, is stable in a wedge-shaped pressure–temperature field with limits of 1 to 1,200 bar pressure, 1,060 to 1,160 °C, and melt water contents of ~2 to >3.5 wt%. These results are consistent with the field-based temperature measurements discussed above, and with the range of total water contents measured for glass inclusions in this study. An important application of this phase diagram to Parícutin is that abrupt decreases of melt total water contents over

the observed range (from 4 to 1.8 wt%) related to decompressive degassing would not result in any change in the stable mineral assemblage. Such a decrease in melt water content would likely change the phase proportions and compositions, but such effects could not be identified in this study.

Carbonate

Studies of vapor/melt partitioning at upper-crustal pressures indicate that carbon strongly favors the vapor (Holloway and Blank 1994). It is not surprising, therefore, in a system that shows other signs of having been variably degassed, to find glass inclusions with low C abundances. As listed in Table 8, only 2 of the 13 analyzed Parícutin glass inclusions have carbonate abundances above the detection limit of ~50 ppm, and only one of these (108135-A) shows consistency in the concentrations calculated for the two peaks of the doublet. Importantly, the two glass inclusions with detectable carbonate also have the highest measured total water contents (4.0 wt%) and among the highest SO_3^t values (Fig. 9b). Thus, these two inclusions provide the best insight into the primary volatile contents of Parícutin melts prior to upper crustal degassing.

Complementary results have been obtained in other studies of mafic glass inclusions from subduction-related volcanoes. In their study of glass inclusions in Xitle tephra, Cervantes and Wallace (2001) also found detectable carbonate only in two inclusions with the highest H_2O contents. In mafic glass inclusions from Vulcano, Italy, Gioncada et al. (1998) observed relatively high H_2O, S, and Cl contents, but carbonate levels below FTIR detection. Roggensack et al. (1997) investigated volatiles in glass inclusions at Cerro Negro, Nicaragua, and found that inclusions from the largely effusive eruption of 1995 had lower H_2O and carbonate contents than those from the explosive eruption of 1992. The simplest interpretation of all these results is that the glass inclusions with low carbonate contents, the dominant form of carbon in these basaltic melt systems, underwent deep crustal degassing prior to inclusion entrapment. Carbon concentrations below the FTIR detection limit are also commonly reported from glass inclusions in silica-rich pumices from subduction-related volcanoes, such as rhyodacites from the cataclysmic 6845 year B.P. eruption at Mount Mazama, USA (Bacon et al. 1992), and rhyodacites erupted in 1883 from Krakatau, Indonesia (Mandeville et al. 1998).

Sulfur and chlorine

Vapor–melt partitioning of both chlorine and sulfur in oxidized systems like Parícutin strongly favor the vapor (Carroll and Webster 1994). Concentrations of SO_3^t (0.30–0.01 wt%) in Parícutin glass inclusions show systematic declines with increasing SiO_2 that project toward the low concentrations in the matrix glasses (Fig. 9b). The total range of Cl values is small (0.11–0.07 wt%), and although Cl also appears to decline with increasing SiO_2 (Fig. 9c), the relatively large error on the Cl measurements reduces the significance of this observation. These declines probably reflect a combination of progressive degassing during magmatic ascent and assimilation of S- and Cl-poor crustal rocks. It is surprising that no correlation is apparent between total sulfur content and total water content for the Parícutin glass inclusions, because variations in both parameters are thought to be related to degassing during magmatic ascent. Measurement of the S-K_α peak position to establish the percentage of sulfate relative to total sulfur in the glass inclusions did not produce interpretable results, as no systematic variations of percent sulfate are evident in plots versus eruption date or any glass compositional variable. Two factors appear to have compromised evaluation of the sulfate/sulfide ratio in the glass inclusions: (1) the analytical conditions and glass sulfur contents imposed a relatively high 1σ average uncertainty of $\pm 17\%$ on these measurements; (2) a 10 μm beam diameter was used, and may have caused oxidation of sulfide to sulfate during analysis of the most hydrous glasses.

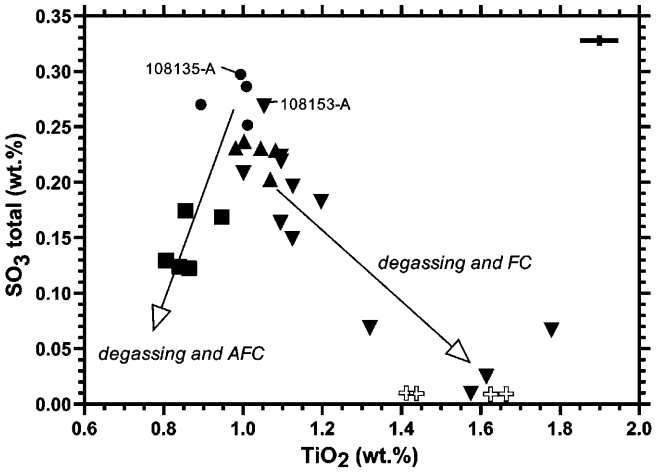

Fig. 10 Concentrations of TiO_2 versus total sulfur as SO_3 for Parícutin glass inclusions and matrix glasses. Data are normalized as discussed in Fig. 9. *Arrows* show two differentiation trends to lower S contents away from the most primitive glass inclusions, including the two with FTIR-detectable carbonate, which are labeled. The trend to elevated TiO_2, recorded in some stage-2 inclusions from sample 108153 and in all four matrix glasses, is consistent with degassing and fractional crystallization (*FC*). The trend to lower TiO_2, found in some stage-3 inclusions from sample 116301-4, is consistent with degassing, fractional crystallization, and crustal assimilation (*AFC*). *Error bars* as in Fig. 7

A plot of TiO_2 versus SO_3^t in Parícutin glasses (Fig. 10) is instructive because it illustrates the two different processes that appear to have played roles in reducing melt sulfur contents: decompressive degassing and fractional crystallization for glass inclusions from stage-2 sample 108153, and the addition of crustal

contamination for stage-3 sample 116301-4. The two inclusions with detectable carbonate lie near the high-S apex of these two trends, consistent with their interpretation as the least degassed glasses analyzed.

Depths of inclusion entrapment

The two least-degassed inclusions (108135-A and 108153-A) contain 4.0 wt% H_2O, 248–296 ppm CO_2, 0.27 wt% SO_3^t, and 0.09–0.10 wt% Cl. Estimates for the minimum pressure of entrapment of these inclusions can be made by extrapolation of isobars for the solubility of H_2O and CO_2 in vapor-saturated basaltic liquids at 1,200 °C (Dixon and Stolper 1995). This approach indicates minimum entrapment pressures of about 2,300 and 2,450 bar for 108135-A and 108153-A, respectively, equivalent to depths of ~9.0 and 9.6 km for a magmatic density of 2,600 g/l. The bubble in 108135-A represents ~3.1% of the inclusion volume, whereas the bubble in 108153-A represents ~8.1 vol% of that inclusion (Table 2). As discussed by Anderson (1973) and Anderson and Brown (1993), glass inclusions like 108135-A, with a bubble volume of only a few percent, were probably either bubble free or contained a single small vapor bubble in the melt at the time of entrapment. During eruptive decompression, shrinkage bubbles nucleated in the formerly bubble-free inclusions, and the small preexisting bubbles of the latter type expanded, both processes due to the greater thermal contraction of the melt upon eruptive cooling compared to the surrounding host olivine. Glass inclusions like 108153-A with its 8.1 vol% bubble, in contrast, must have either (1) leaked melt and had the bubble expand, (2) undergone large amounts of host mineral crystallization, or (3) contained a bubble of significant size (here ~5%) at the time of melt entrapment (Anderson 1973). As discussed earlier, the first two processes can probably be ruled out for the Parícutin glass inclusions of this study. Thus, the size of the bubble in 108153-A indicates that it probably represents entrapment of a vapor-saturated melt.

For the other glass inclusions, in which carbonate was below FTIR detection, estimates of minimum entrapment pressure can be calculated from the total water contents using the water solubility model of Moore et al. (1998). It is assumed that the melts were saturated with water at the time of entrapment. Given the relatively high water contents of the Parícutin glass inclusions (1.8–4.0 wt%), the ascending melts would have eventually become water saturated in the upper crust. Also the water-saturated phase-equilibrium experiments of Moore and Carmichael (1998) closely reproduce the phase assemblages of the Parícutin magmas in the pressure range 1 to 1,200 bar. H_2O-saturation pressures are listed for each glass inclusion in Table 7. These pressures range from 340 to 1,310 bar, equivalent to depths below the volcano of 1.3 to 5.1 km, again assuming an average magmatic density of 2,600 g/l.

Implications for the Parícutin plumbing system and magmatic degassing

Through its 9-year lifespan, Parícutin's magma system alternately (and at times simultaneously) fed highly explosive tephra eruptions from the summit crater and non-explosive lava eruptions from vents at the northeast and southwest bases of the cone (Luhr and Simkin 1993). This behavior was the most dramatic evidence of subterranean gas separation from the magma. Several observations from this study also indicate the importance of degassing in the Parícutin magmas prior to eruption: (1) the wide range of total water contents measured for glass inclusions from single tephra samples; (2) carbonate concentrations detectable by FTIR (>50 ppm equivalent CO_2) in only 2 of 13 inclusions, which probably reflect stripping of carbonate from the melt during mid-crustal degassing; (3) S concentrations that decline with increasing SiO_2 and K_2O in the glass inclusions, indicating that degassing accompanied progressive magmatic differentiation by combined fractional crystallization and crustal assimilation.

Where and when did magmatic degassing occur beneath Parícutin? Krauskopf (1948a) made key observations on this subject and presented a model (his Fig. 13) according to which the magma that erupted as lava from the flank vents had first degassed in the central vent during explosive episodes. In the process it lost its water and sulfur, and then fell back to flow through a tortuous network of channels toward the flank lava vents. By the time the lava emerged from the flank vents, it still retained significant Cl, commonly detected by the odor of HCl at fumaroles and hornitos associated with the flank lavas, especially those with characteristic blue flames. Degassing was likely a quasi-continuous phenomenon during magmatic ascent, with glass inclusions trapped at different levels. The two inclusions with detectable CO_3^{2-} also have the highest H_2O contents and among the highest SO_3^t contents, and record the deepest entrapment pressures (≥2,300–2,450 bar) equivalent to depths of ≥9.0–9.6 km. Water contents measured for other glass inclusions indicate saturation pressures of ≥340–1,380 bar, and minimum depths of entrapment of 1.3–5.1 km. Thus, glass inclusions trapped in Parícutin olivine crystals provide a glimpse of the complex interplay among degassing, crystallization, and assimilation during ascent of the magmas through the upper third of the crust just prior to eruption.

Acknowledgements On numerous occasions, Paul Wallace patiently provided instruction and advice on all aspects of sample preparation and FTIR analysis. His input was critical to the completion of this work. Paul also gave an informal review of the manuscript that was very helpful. Rebecca Lange kindly permitted use of unpublished partial molar volume data for silicate melts in the calculation of glass densities. At the Smithsonian, Tim Gooding and Tim Rose helped in the development of sample preparation techniques, Amelia Logan assisted in development of analytical routines on the electron microprobe, and Anne Peslier and Richard Wysoczanski offered advice on FTIR spectroscopy. Reviews by Kurt Roggensack and an anonymous individual were most helpful

in pointing out some misinterpretations and leading to significant improvements. Thanks to all of you for your assistance.

References

Anderson AT Jr (1973) The before-eruption water contents of some high-alumina magmas. Bull Volcanol 37:530–552

Anderson AT Jr (1991) Hourglass inclusions: theory and application to the Bishop Rhyolite Tuff. Am Mineral 76:530–547

Anderson AT Jr, Brown GG (1993) CO_2 contents and formation pressures of some Kilauean melt inclusions. Am Mineral 78:794–803

Bacon CR, Newman S, Stolper E (1992) Water, CO_2, Cl, and F in melt inclusions in phenocrysts from three Holocene explosive eruptions, Crater Lake, Oregon. Am Mineral 77:1021–1030

Bannister V, Roeder P, Poustovetov A (1998) Chromite in the Parícutin lava flows (1943–1952). J Volcanol Geotherm Res 87:151–171

Bartholomew RF, Butler BL, Hoover HL, Wu CK (1980) Infrared spectra of a water-containing glass. J Am Ceram Soc 63:481–485

Carroll MR, Rutherford MJ (1988) Sulfur speciation in hydrous experimental glasses of varying oxidation states: results from measured wavelength shifts of sulfur X-rays. Am Mineral 73:845–849

Carroll MR, Webster JD (1994) Solubilities of sulfur, noble gases, nitrogen, chlorine, and fluorine in magmas. In: Carroll MR, Holloway JR (eds) Volatiles in magmas, vol 30, Mineral Soc Am, Reviews in Mineralogy, pp 231–279

Cervantes P, Wallace P (2001) Magma degassing and basaltic eruption styles: a case study of ~2000 yr BP Xitle volcano in central Mexico. J Volcanol Geotherm Res (in press)

Cioni R (2000) Volatile content and degassing processes in the AD 79 magma chamber at Vesuvius (Italy). Contrib Mineral Petrol 140:50–54

DePaolo DJ (1981) Trace element and isotopic effects of combined wallrock assimilation and fractional crystallization. Earth Planet Sci Lett 53:189–202

Dixon JE, Pan V (1995) Determination of the molar absorptivity of dissolved carbonate in basanitic glass. Am Mineral 80:1339–1342

Dixon JE, Stolper EM (1995) An experimental study of water and carbon dioxide solubilities in mid-ocean ridge basaltic liquids. Part II: Applications to degassing. J Petrol 36:1633–1646

Dixon JE, Stolper EM, Holloway JR (1995) An experimental study of water and carbon dioxide solubilities in mid-ocean ridge basaltic liquids. Part I: Calibration and solubility models. J Petrol 36:1607–1631

Eggler DH (1972) Water-saturated and undersaturated melting relations in a Parícutin andesite and an estimate of water content in the natural magma. Contrib Mineral Petrol 34:261–271

Fedotov SA, Balesta ST, Dvigalo VN, Razina AA, Flerov GB, Chirkov AM (1991) New Tolbachik volcanoes. In: Fedotov SA, Masurenkov YP (eds) Active volcanoes of Kamchatka, vol 1. Nauka Publishers, Moscow, pp 275–279

Fine G, Stolper E (1985) The speciation of carbon dioxide in sodium aluminosilicate glasses. Contrib Mineral Petrol 91:105–121

Fine G, Stolper E (1986) Dissolved carbon dioxide in basaltic glasses: concentrations and speciation. Earth Planet Sci Lett 76:263–278

Foshag WF (1943) Las fumarolas del Parícutin. In: El Parícutin, Estado de Michoacán, Instituto de Geología, Univ Nac Auton Méx, pp 95–100

Foshag WF, González-Reyna JR (1956) Birth and development of Parícutin volcano, México. US Geol Surv Bull 965D:355–489

Fries C Jr (1953) Volumes and weights of pyroclastic material, lava, and water erupted by Parícutin volcano, Michoacán, México. Trans Am Geophys Union 34(4):603–616

Fries C Jr, Gutiérrez C (1950a) Activity of Parícutin volcano from August 1, 1948 to June 30, 1949. Trans Am Geophys Union 31(3):406–418

Fries C Jr, Gutiérrez C (1950b) Activity of Parícutin volcano from July 1 to December 31, 1949. Trans Am Geophys Union 31(5):732–740

Fries C Jr, Gutiérrez C (1951a) Activity of Parícutin volcano from January 1 to June 30, 1950. Trans Am Geophys Union 32(2):212–221

Fries C Jr, Gutiérrez C (1951b) Activity of Parícutin volcano from July 1 to December 31, 1950. Trans Am Geophys Union 32(4):572–581

Fries C Jr, Gutiérrez C (1952a) Activity of Parícutin volcano from January 1 to June 30, 1951. Trans Am Geophys Union 33(1):91–100

Fries C Jr, Gutiérrez C (1952b) Activity of Parícutin volcano from July 1 to December 31, 1951. Trans Am Geophys Union 33(5):725–733

Fries C Jr, Gutiérrez C (1954) Activity of Parícutin volcano during the year 1952. Trans Am Geophys Union 35(3):486–494

Gioncada A, Clocchiatti R, Sbrana A, Bottazzi P, Massare D, Ottolini L (1998) A study of melt inclusions at Vulcano (Aeolian Islands, Italy): insights on the primitive magmas and on the volcanic feeding system. Bull Volcanol 60:286–306

Hernández-Velasco JA (1943) Analisis de lavas, arenas, cenizas, sublimados, y gases procedentes del volcán, practicados en los laboratorios de Instituto. In: El Parícutin, Estado de Michoacán, Instituto de Geología, Univ Nac Auton Méx, pp 135–137

Holloway JR, Blank JG (1994) Application of experimental results to C–O–H species in natural melts. In: Carroll MR, Holloway JR (eds) Volatiles in magmas, vol 30, Mineral Soc Am, Reviews in Mineralogy, pp 187–230

Ihinger PD, Hervig RL, McMillan PF (1994) Analytical methods for volatiles in glasses. In: Carroll MR, Holloway JR (eds) Volatiles in magmas, vol 30, Mineral Soc Am, Reviews in Mineralogy, pp 67–121

Jarosewich E, Nelen JA, Norberg JA (1980) Reference samples for electron microprobe analysis. Geostand Newsl 4:43–47

Johnson MC, Anderson AT Jr, Rutherford MJ (1994) Pre-eruptive volatile contents of magmas. In: Carroll MR, Holloway JR (eds) Volatiles in magmas, vol 30, Mineral Soc Am, Reviews in Mineralogy, pp 281–330

Kennedy GC (1946) Activity of Parícutin volcano April 12 to May 3, 1946. Trans Am Geophys Union 27(3):410–411

Krauskopf KB (1948a) Mechanism of eruption at Parícutin volcano, México. Geol Soc Am Bull 59:711–732

Krauskopf KB (1948b) Lava movement at Parícutin volcano, México. Geol Soc Am Bull 59:1267–1283

Krauskopf KB, Williams H (1946) The activity of Parícutin during its third year. Trans Am Geophys Union 27(3):406–410

Lange RA, Carmichael ISE (1990) Hydrous basaltic andesites associated with minette and related lavas in western Mexico. J Petrol 31:1225–1259

Lange RA, Carmichael ISE (1991) A potassic volcanic front in western Mexico: the lamprophyric and related lavas of San Sebastian. Geol Soc Am Bull 103:928–940

Luhr JF (1997) Extensional tectonics and diverse primitive volcanic rocks in the western Mexican Volcanic Belt. Can Mineral 35:473–500

Luhr JF, Carmichael ISE (1985) The 1759–1774 eruption of Jorullo Volcano, Michoacán, México: the earliest stages of fractionation in calc-alkaline magmas. Contrib Mineral Petrol 90:142–161

Luhr JF, Housh TB (1993) A possible parental basalt to the Parícutin suite: the "early bomb" of Anguiano and Martínez. EOS Trans Am Geophys Union 74(43):673

Luhr JF, Simkin T (1993) Parícutin: the volcano born in a Mexican cornfield. Geoscience Press, Phoenix

Luhr JF, Allan JF, Carmichael ISE, Nelson SA, Hasenaka T (1989) Primitive calc-alkaline and alkaline volcanic rock types from the western Mexican Volcanic Belt. J Geophys Res 94(B4):4515–4530

Mandeville CW, Sasaki A, Saito G, Faure K, King R, Hauri E (1998) Open-system degassing of sulfur from Krakatau 1883 magma. Earth Planet Sci Lett 160:709–722

Matthews SJ, Moncrieff DHS, Carroll MR (1999) Empirical calibration of the sulphur valence oxygen barometer from natural and experimental glasses: methods and applications. Mineral Mag 63(3):421–431

McBirney AR, Taylor HP Jr, Armstrong RL (1987) Parícutin re-examined: a classic example of crustal assimilation in calc-alkaline magma. Contrib Mineral Petrol 95:4–20

Metrich N, Clocchiatti R (1996) Sulfur abundance and its speciation in oxidized alkaline melts. Geochim Cosmochim Acta 60(21):4151–4160

Moore GM, Carmichael ISE (1998) The hydrous phase equilibria (to 3 kbar) of an andesite and basaltic andesite from western Mexico: constraints on water content and conditions of phenocryst growth. Contrib Mineral Petrol 130:304–319

Moore GM, Vennemann T, Carmichael ISE (1998) An empirical model for the solubility of water in magmas to 3 kilobars. Am Mineral 83:36–42

Nakamoto K (1978) Infrared and Raman spectra of inorganic and coordination compounds, 3rd edn. Wiley, New York

Nilsson K, Peach CL (1993) Sulfur speciation, oxidation state, and sulfur concentration in backarc magmas. Geochim Cosmochim Acta 57:3807–3813

NIST (National Institute of Standards and Technology) (1995) Standard reference materials catalog 1995–96, NIST Spec Pub 260:112

Peck LC (1964) Systematic analysis of silicates. US Geol Surv Bull 1170

Roggensack K, Hervig RL, McKnight SB, Williams SN (1997) Explosive basaltic volcanism from Cerro Negro volcano: influence of volatiles on eruptive style. Science 277:1639–1642

Schmitter E (1943) Estudio petrographico de lavas y productos piroclasticos. In: El Parícutin, Estado de Michoacán, Instituto de Geología, Univ Nac Auton Méx, pp 113–131

Scholze H (1959) Der Einbau des Wassers in Gläsern. Glastech Ber 32:81–88, 142–145, 278–281

Scholze H (1960) Zur Frage der Untersheidung zwischen H_2O-Moleceln und OH-Gruppen in Gläsern und Mineralen. Naturwiss 47:226–227

Segerstrom K, Gutiérrez C (1947) Activity of Parícutin volcano from May 4 to September 8, 1946. Trans Am Geophys Union 28(4):559–566

Siebe C (2000) Age and archaeological implications of Xitle volcano, southwestern Basin of Mexico-City. J Volcanol Geotherm Res 104:45–64

Smith BC (1996) Fundamentals of Fourier transform infrared spectroscopy. CRC Press, Boca Raton

Spera FJ (1984) Some numerical experiments on the withdrawal of magma from crustal reservoirs. J Geophys Res 89:8222–8236

Stolper E (1982) Water in silicate glasses: an infrared spectroscopic study. Contrib Mineral Petrol 81:1–17

Ulmer P (1989) The dependence of Fe^{2+}–Mg cation-partitioning between olivine and basaltic liquid on pressure, temperature, and composition: an experimental study to 30 kbars. Contrib Mineral Petrol 101:261–273

Wallace P, Carmichael ISE (1992) Alkaline and calc-alkaline lavas near Los Volcanes, Jalisco, Mexico: geochemical diversity and its significance in volcanic arcs. Contrib Mineral Petrol 111:423–439

Wallace P, Carmichael ISE (1994) S speciation in submarine basaltic glasses as determined by measurements of SKα X-ray wavelength shifts. Am Mineral 79:161–167

Wallace P, Carmichael ISE, Righter K, Becker TA (1992) Volcanism and tectonism in western Mexico: a contrast in style and substance. Geology 20:625–628

Wilcox RE (1947a) Activity of Parícutin volcano from September 18 to November 30, 1946. Trans Am Geophys Union 28(4):567–572

Wilcox RE (1947b) Activity of Parícutin volcano from December 1, 1946 to March 31, 1947. Trans Am Geophys Union 28(5): 725–731

Wilcox RE (1948a) Activity of Parícutin volcano from April 1 to July 31, 1947. Trans Am Geophys Union 29(1):69–74

Wilcox RE (1948b) Activity of Parícutin volcano from December 1, 1947 to March 31, 1948. Trans Am Geophys Union 29(3):355–360

Wilcox RE (1954) Petrology of Parícutin volcano, México. US Geol Surv Bull 965C:281–353

Wilcox RE, Gutiérrez C (1948) Activity of Parícutin volcano from April 1 to July 31, 1948. Trans Am Geophys Union 29(6):877–881

Wilcox RE, Shoup-Oropeza S (1948) Activity of Parícutin volcano from August 1 to November 30, 1947. Trans Am Geophys Union 29:74–79

Zhang Y, Zhengjiu X, Behrens H (2000) Hydrous species geospeedometer in rhyolite; improved calibration and application. Geochim Cosmochim Acta 64(19):3347–3355

Zies EG (1946) Temperature measurements at Parícutin volcano. Trans Am Geophys Union 27:178–180